

1 scGPT: Towards Building a Foundation Model for Single-Cell  
2 Multi-omics Using Generative AI

3 Haotian Cui<sup>1,2,3\*</sup>, Chloe Wang<sup>1,2,3\*</sup>, Hassaan Maan<sup>1,3,4</sup>,  
Kuan Pang<sup>2,3</sup>, Fengning Luo<sup>2,3</sup>, Bo Wang<sup>1,2,3,4,5,6†</sup>

4 <sup>1</sup>Peter Munk Cardiac Centre, University Health Network, Toronto, ON, Canada

5 <sup>2</sup>Department of Computer Science, University of Toronto, Toronto, ON, Canada

6 <sup>3</sup>Vector Institute, Toronto, ON, Canada

7 <sup>4</sup>Department of Medical Biophysics, University of Toronto, Toronto, ON, Canada

8 <sup>5</sup>Department of Laboratory Medicine and Pathobiology, University of Toronto, Toronto, ON,  
9 Canada

10 <sup>6</sup>AI Hub, University Health Network, Toronto, ON, Canada

11 **Abstract**

12 Generative pre-trained models have achieved remarkable success in various domains such as nat-  
13 ural language processing and computer vision. Specifically, the combination of large-scale diverse  
14 datasets and pre-trained transformers has emerged as a promising approach for developing foun-  
15 dation models. Drawing parallels between linguistic constructs and cellular biology — where texts  
16 comprise words, similarly, cells are defined by genes — our study probes the applicability of founda-  
17 tion models to advance cellular biology and genetics research. Utilizing the burgeoning single-cell  
18 sequencing data, we have pioneered the construction of a foundation model for single-cell biology,  
19 scGPT, which is based on generative pre-trained transformer across a repository of over 33 million  
20 cells. Our findings illustrate that scGPT, a generative pre-trained transformer, effectively distills  
21 critical biological insights concerning genes and cells. Through the further adaptation of transfer  
22 learning, scGPT can be optimized to achieve superior performance across diverse downstream ap-  
23 plications. This includes tasks such as cell-type annotation, multi-batch integration, multi-omic  
24 integration, genetic perturbation prediction, and gene network inference. The scGPT codebase is  
25 publicly available at <https://github.com/bowang-lab/scGPT>.

26 **1 Main**

27 Single-cell RNA sequencing (scRNA-seq), by enabling intricate characterization of distinct cell  
28 types and advancing our understanding of disease pathogenesis, paves the way for cellular het-  
29 erogeneity exploration, lineage tracking, pathogenic mechanism elucidation, and, ultimately, per-

---

\*These authors contributed equally.

†Corresponding author. Email: bowang@vectorinstitute.ai

sonalized therapeutic strategies [1, 2, 3, 4]. The broad-scale application of scRNA-seq has led to comprehensive data atlases like the Human Cell Atlas, which now encompasses tens of millions of cells [5, 6, 7, 8]. Furthermore, such “omic” data is expanding exponentially. Recent sequencing technology advancements in the diversity of data modalities extend our understanding beyond genetics to epigenetics, transcriptomics, and proteomics, thus providing multi-modal insights [9, 10]. These breakthroughs have also raised new research questions such as reference mapping, perturbation prediction, and multi-omic integration [11, 12, 13, 14, 15]. Given the rapid expansion of sequencing data, it is critical to parallelly develop methodologies capable of effectively harnessing, enhancing, and adapting to these burgeoning developments.

One promising approach to address this challenge is the generative pre-training of foundation models [16, 17]. Generative pre-training has recently achieved unprecedented success across various fields by learning from extensive datasets. The most well-known applications include computer vision and natural language generation (NLG) [18, 19, 20]. These foundation models such as DALL-E2 and GPT-4 follow a paradigm of pre-training transformers on large-scale diverse datasets [19, 20] that can be readily customized for a variety of downstream tasks and scenarios. More interestingly, these generative pre-trained models consistently outperform task-specific models trained from scratch [21, 22, 23]. This indicates a task-agnostic understanding of knowledge in these domains, inspiring us to explore its adoption for sing-cell omics research. However, current machine-learning-based methods in single-cell research are rather scattered, with specific models dedicated to distinct analysis tasks [24, 25, 26]. As a result, the datasets used in each study are often limited in breadth and scale [8]. To confront this limitation, there is a need for a foundation model that is pre-trained on large-scale data and can comprehend the complex interactions between genes across diverse tissues. We expect that such a model would provide a solid foundation and contribute to the discovery of new biological insights by leveraging the knowledge learned from millions of sequenced cells.

To enhance the modeling of large-scale data of single-cell sequencing, we draw inspiration from the self-supervised pre-training workflow in NLG. The self-attention transformer has been verified as an effective and efficient architecture to model input tokens of words [27]. While texts are made up of words, cells can be characterized by genes and the protein products they encode. By learning gene and cell embeddings simultaneously, akin to word and sentence embeddings in NLG, we can better comprehend the characteristics of cells based on the genes they express. Moreover, the flexible nature of transformer input tokens enables easy incorporation of additional features and meta information.

In this work, we present the first attempt to build a single-cell foundation model, scGPT, by generative pre-training on over 33 million cells. We introduce new techniques to address the methodology and engineering challenges of pre-training on large-scale single-cell omic data. To handle large-scale data, we use an in-memory data structure that allows fast access to store hundreds of datasets. We establish a unified generative pre-training workflow specifically for the non-sequential omic data, and adapt the transformer architecture to simultaneously learn cell and gene representations. Additionally, we provide common pipelines with task-specific objectives for model fine-tuning, designed to facilitate the application of the pre-trained model across a range of downstream tasks.

Our model, scGPT, demonstrates the transformative potential of the single-cell foundation model through three key aspects. First, scGPT represents the first large-scale *generative* foundation models that enable transfer learning across a diverse range of downstream tasks. By achieving state-of-the-art performance on cell type annotation, genetic perturbation prediction, batch correction, and multi-omic integration, we showcase the effectiveness of the “pre-training universally, fine-tuning on demand” approach as a generalist solution for computational applications in single-

78 cell omics. Notably, scGPT is the only foundation model that can integrate multiple single-  
79 cell omics including scATAC-seq data. Second, through the comparison of gene embeddings and  
80 attention weights between the fine-tuned and raw pre-trained models, scGPT uncovers valuable  
81 biological insights into gene-gene interactions specific to various conditions, such as cell types and  
82 perturbation states. Third, our observations reveal a scaling law: larger pre-training data sizes yield  
83 superior pre-trained embeddings and further lead to improved performance on downstream tasks.  
84 This finding highlights the exciting prospect that foundation models can continuously improve  
85 alongside the expansion of available sequencing data in the research community. Based on these  
86 findings, we envision that the adoption of pre-trained foundation models will greatly expand our  
87 understanding of cellular biology and serve as a solid foundation for future discoveries. The release  
88 of the scGPT models and workflow aims to empower and expedite research in these areas and  
89 beyond.

## 90 2 Results

### 91 2.1 Single-cell transformer foundation model overview

92 Single-cell sequencing enables the profiling of molecular characteristics at the individual cell level.  
93 For instance, scRNA-seq measures the abundance of RNA transcripts, providing insights into cell  
94 identity, developmental stage, and functionality. We introduce scGPT as the first foundation  
95 model in the single-cell domain with a generative pre-training approach. The core model contains  
96 stacked transformer layers with multi-head attention [27] that generate cell and gene embeddings  
97 simultaneously (Online Methods 4.2). scGPT consists of two stages: the initial general-purpose  
98 pre-training on large cell atlases and the follow-up fine-tuning on smaller datasets for specific applica-  
99 tions (Figure 1A-C). In the pre-training stage, we introduce a specially designed attention mask  
100 and generative training pipeline to train scGPT in a self-supervised manner to jointly optimize cell  
101 and gene representations (Online Methods 4.3). This innovative technique successfully addresses  
102 the non-sequential nature of gene expression to adapt to the NLG framework of sequential pre-  
103 dictions. During training, the model gradually learns to generate gene expression of cells based on  
104 cell states or gene expression cues. In the fine-tuning stage, the pre-trained model can be adapted  
105 to new datasets and specific tasks (Online Methods 4.5). We offer flexible fine-tuning pipelines  
106 suitable for a variety of essential downstream tasks in single-cell research, including scRNA-seq  
107 integration with batch correction, cell type annotation, multi-omic integration, perturbation pre-  
108 diction, and gene regulatory network inference. These pipelines enable researchers to leverage the  
109 power of scGPT for diverse applications in single-cell analysis.

110 To collect diverse and extensive sequencing data for the self-supervised pre-training of scGPT,  
111 we assembled 33 million scRNA-seq data of human cells under normal (non-disease) conditions, ob-  
112 tained via the CELLxGENE collection [28] (Figure 1D). This comprehensive dataset encompasses  
113 a wide range of cell types from 51 organs/tissues and 441 studies, providing a rich representation  
114 of cellular heterogeneity across the human body. After pre-training, we visualized the scGPT  
115 cell embeddings on 10% of the human cells out of the 33 million data using UMAP visualization  
116 [29] (Figure 1E). The resulting UMAP plot exhibits intriguing clarity, with cell types accurately  
117 represented by distinct colors at localized regions and clusters. Considering the inclusion of over  
118 400 studies in the dataset, this demonstrates the remarkable capability of pre-training to mitigate  
119 technical batch effects.

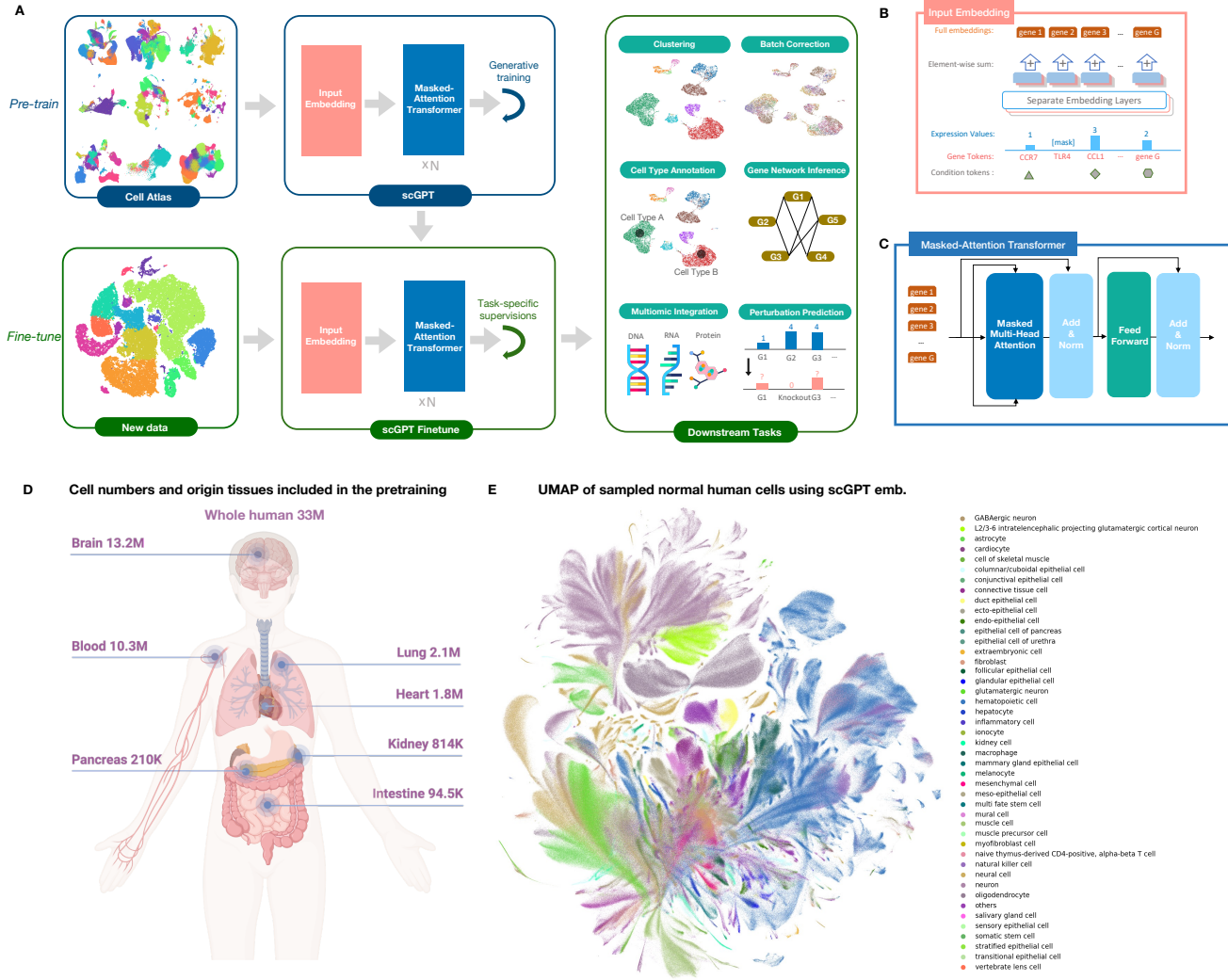


Figure 1: Model Schematic. (A) The workflow of scGPT. The model is generatively pre-trained on large-scale scRNA-seq data from cell atlases. For downstream applications, the pre-trained model parameters can be fine-tuned on new data. The core component of scGPT contains stacked transformer blocks with specialized attention masks for generative training. We applied scGPT on a variety of tasks including cell type annotation, batch correction, multi-omic integration, genetic perturbation prediction, and gene network inference. (B) The detailed view of the input data embeddings. The input contains three layers of information, gene tokens, expression values, and condition tokens (modality, batch, perturbation conditions, etc.). (C) The detailed view of the scGPT transformer layer. We introduced a specially designed attention mask in the Masked Multi-Head Attention block to conduct generative pre-training on single-cell sequencing data. (D) The diagram illustrating the size of training data and the organs of origin. The scGPT whole-human model was pre-trained on the scRNA-seq data of 33 million normal human cells. (E) UMAP visualization of the pre-trained scGPT cell embeddings (a random 10% subset), colored by major cell types.

120

## 2.2 scGPT improves the precision of cell type annotation

121  
122  
123  
124  
125  
126  
127

Cell type annotation is a crucial step in single-cell analysis, enabling the identification and characterization of distinct cell populations within sequenced tissues. While several methods have been proposed for cell annotation [30, 31, 32], they often require dimension reduction prior to model input, which can lead to information loss. In contrast, scGPT's transformer model offers an advantage by directly accepting gene expression as input without the need for prior dimension reduction. This approach provides improved reliability and accuracy as demonstrated in our subsequent analyses.

128  
129  
130  
131  
132  
133  
134  
135  
136

To evaluate the performance of scGPT for cell-type annotation, we conducted extensive experiments on a variety of diverse datasets. Firstly, we adapted scGPT to predict cell types in a human pancreas (hPancreas) dataset. The model was fine-tuned on a reference data partition and used to predict on a held-out query data partition. We visualized the predictions in Figure 2A. Notably, scGPT achieved high precision ( $> 0.8$ ) for most cell types shown in the confusion matrix (Figure 2B), only except for rare cell types with extremely low cell numbers in the reference partition. For example, fewer than 50 cells belong to the mast and MHC class II cell types out of the 106,000 cells in the reference set. Figure 2C visualizes the cell embeddings in the fine-tuned scGPT, which demonstrate high intra-cell-type similarities.

137  
138  
139  
140  
141  
142  
143  
144  
145  
146  
147

Next, we tested the model on a disease dataset of multiple sclerosis (M.S.). The model was fine-tuned on a reference partition of healthy human immune cells and evaluated on the prediction for the cells with M.S. condition (Figure 2D). The fine-tuned model demonstrated strong alignment with the cell type annotations provided by the original study and achieved a high accuracy of around 0.85 (Figure 2I,J). Additionally, to investigate the impact of pre-training on fine-tuning, we separately pre-trained scGPT models on smaller subsets of the collected normal human cells, including 30K, 300K, and 3M cells, respectively. Interestingly, the results revealed a *scaling law*, where larger pre-training datasets consistently contribute to better fine-tuning performance (Figure 2E,F). This can be exemplified by the outlined regions in Figure 2E, where the fine-tuned model gradually gained the near-perfect capability of distinguishing expiatory neurons at different cortical layers as the pretraining dataset increased.

148  
149  
150  
151  
152  
153  
154  
155  
156  
157

Furthermore, we applied the model to a more challenging scenario for generalization across disease types, using a tumor-infiltrating myeloid dataset (Mye.) [33]. The model was fine-tuned on six cancer types in a reference data partition (Online Methods 4) and evaluated on the query partition of three unseen cancer types (Figure 2G). The results demonstrated high precision in distinguishing immune cell subtypes (Figure 2H,K), and the cell embeddings exhibited clear separability among different cell types (Figure 2L). The predictions reached high precision ( $\geq 0.7$ ) for most cell types. Finally, we benchmarked the fine-tuned scGPT against two other recent transformer-based methods, TOSICA [34] and scBert [35], across the three datasets (Online Methods 4.7). scGPT constantly outperforms the other methods on all classification metrics, including *Accuracy*, *Precision*, *Recall*, and *MacroF1* (Figure 2J).

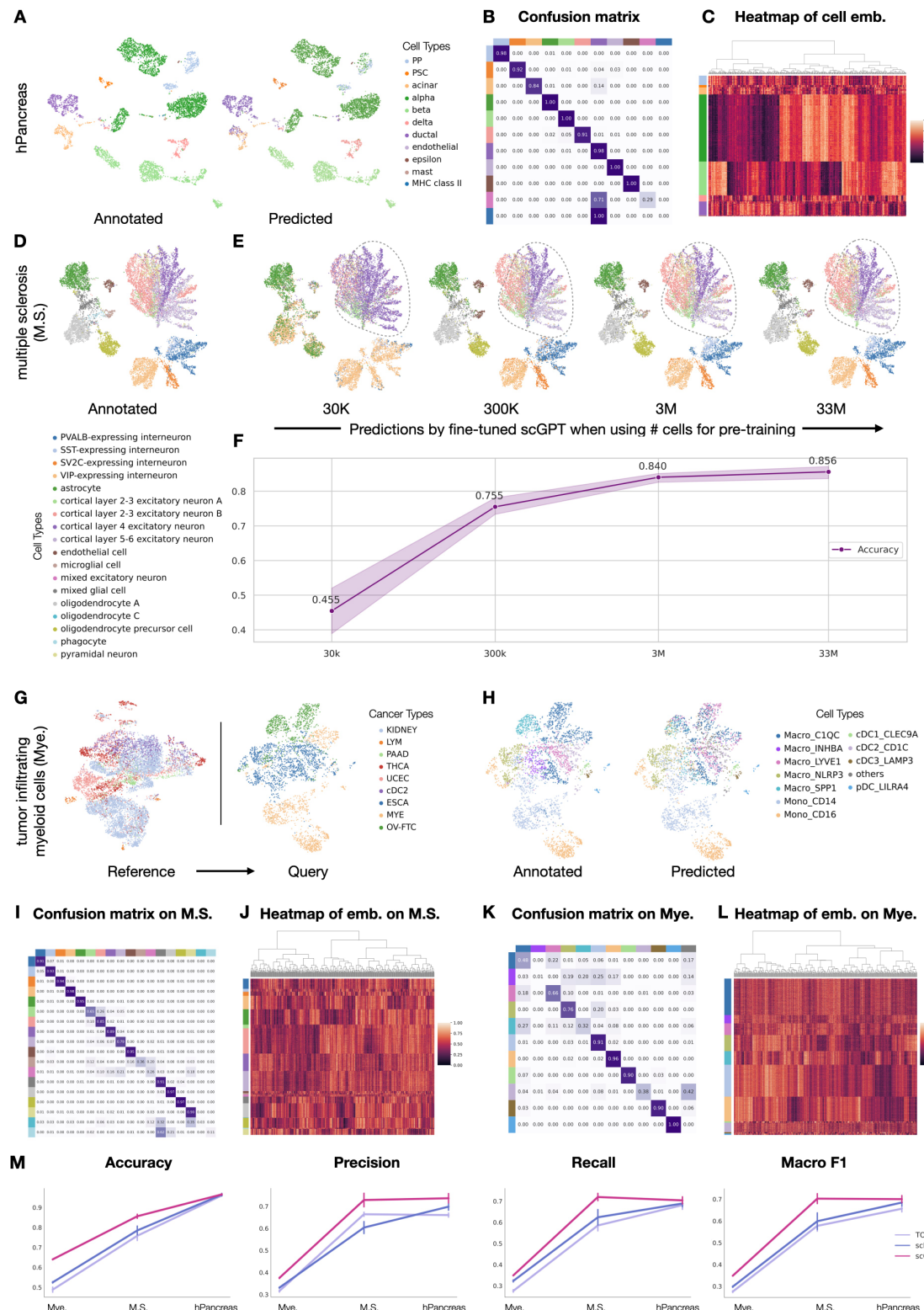


Figure 2: (Continued on the following page.)

Figure 2: Cell type annotation results using scGPT. (A) UMAP of the gene expression of cells from the hPancreas dataset, colored by the *cell types* annotated in the original study (left) and by the *cell types* predicted by the fine-tuned scGPT (right). On the hPancreas dataset, (B) The confusion matrix between predicted and annotated cell types, (C) the heatmap of the 512-dimensional cell embeddings in scGPT. (D) UMAP of the multiple sclerosis (M.S.) dataset colored by the *cell types* annotated in the original study. (E) UMAP of M.S. colored by the predictions of four fine-tuned scGPT models using different pre-training models. From left to right, 30K, 300K, 3M, and 33M normal human cells were used during pre-training. (F) The prediction accuracy increases as the number of cells grows in pre-training. (G) UMAP visualization of the tumor-infiltrating myeloid dataset (Mye.), colored by *cancer types*. scGPT was fine-tuned on the reference partition (left) and evaluated on the query partition (right). These two data partitions contain distinct cancer types. (H) UMAP colored by the cell types annotated in the original study (left) and by the scGPT predicted *cell types*. (I,K) The confusion matrices between predicted cell types and actual annotations on M.S. and Mye., respectively. (J,L) Heatmaps showing the 512-dimensional cell embeddings in scGPT for cells in M.S. and Mye., respectively. (M) scGPT’s performance on Mye., M.S., and the hPancreas datasets.

158

## 2.3 scGPT predicts unseen genetic perturbation responses

159  
160  
161  
162  
163  
164  
165  
166  
167  
168  
169

Recent advancements in sequencing and gene editing techniques have greatly facilitated large-scale perturbation experiments, allowing for the investigation of cellular responses to various genetic perturbations. The approach holds immense promise for uncovering novel gene interactions and advancing regenerative medicine. However, the vast combinatorial space of potential gene perturbations quickly surpasses the practical limits of experimental feasibility. To overcome this limitation, scGPT can be employed to leverage the knowledge gained from cellular responses in known experiments and extrapolate them to predict responses in unknown scenarios. The utilization of self-attention mechanisms over the gene dimension enables the encoding of intricate interactions between perturbed genes and the responses of other genes. By leveraging this capability, scGPT can effectively learn from existing experimental data and accurately predict the gene expression following perturbation.

170

### Prediction of Unseen Gene Perturbations

171  
172  
173  
174  
175  
176  
177  
178  
179  
180  
181  
182  
183  
184  
185  
186

For the perturbation prediction task, we evaluated our model using two perturbation datasets of K562 leukemia cell lines: the Adamson Pertub-seq dataset [36] consisting of 87 one-gene perturbations and the Norman Perturb-Seq dataset [37] consisting of 131 two-gene perturbations and 105 one-gene perturbations. To assess scGPT’s perturbation prediction capability, we fine-tuned the model on a subset of perturbations and tested it on perturbations involving unseen genes (Online Methods 4.5). We measured the performance using the Pearson correlation (*corr*) between the predicted and actual expression values after perturbation. We calculated the correlation scores based on the top 20 most significantly changed genes for each perturbation, namely (DE) genes. Additionally, we adopted a variant of the Pearson metric, denoted as *corr*( $\Delta$ ), which measures the correlation based on the magnitude of expression change post-perturbation compared to the control. These evaluations follow the choices from GEARS [38]. See Supplementary Note S.5 for the details on metric calculations. We conducted a performance comparison between scGPT and two other recent methods, GEARS [38] and CPA [39]. Our results demonstrate that scGPT achieves the highest correlation on both datasets (Figure 3A). Additionally, we visualize the predictions for two example perturbations in the Adamson dataset in Figure 3B, where scGPT accurately predicts the trend of expression change for all top 20 DE genes.

187  
188  
189  
190  
191  
192  
193  
194  
195  
196  
197  
198  
199  
200  
201  
202  
203

The ability to predict unseen perturbation responses could expand the scope of perturbation experiments, as depicted in Figure 3C. To explore the expanded space of predicted perturbation responses, we conducted clustering analysis using the Norman dataset to validate the biologically relevant functional signals. The original Perturb-seq study covered 236 one-gene or two-gene perturbations targeting 105 genes. However, considering all possible combinations of these target genes, there are a total of 5,565 potential perturbations. This means that the experimental Perturb-seq only represents 5% of the entire perturbation space. Therefore, we applied the fine-tuned scGPT to expand the perturbation *in-silico* and visualized the predicted mean response for each perturbation in Figure 3D using UMAP. Using the annotations from the original study, we found the perturbation conditions of the same functional groups gathered at nearby regions (Supplementary Figure S4). Next, we clustered the predicted expression using Leiden [40] and mapped each data point with the corresponding perturbed genes. Interestingly, we observed that the clusters exhibited a high association with the “dominant gene” within the perturbation combinations. For example, the circled cluster associated with the *KLF1* gene indicated that the data points in this cluster underwent combined perturbations involving *KLF1* along with another gene (i.e., *KLF1 + X*). Using *KLF1* and *CNN1* clusters as two examples, we further validated that the corresponding predicted expression was exclusively high in these regions (Figure 3E), which

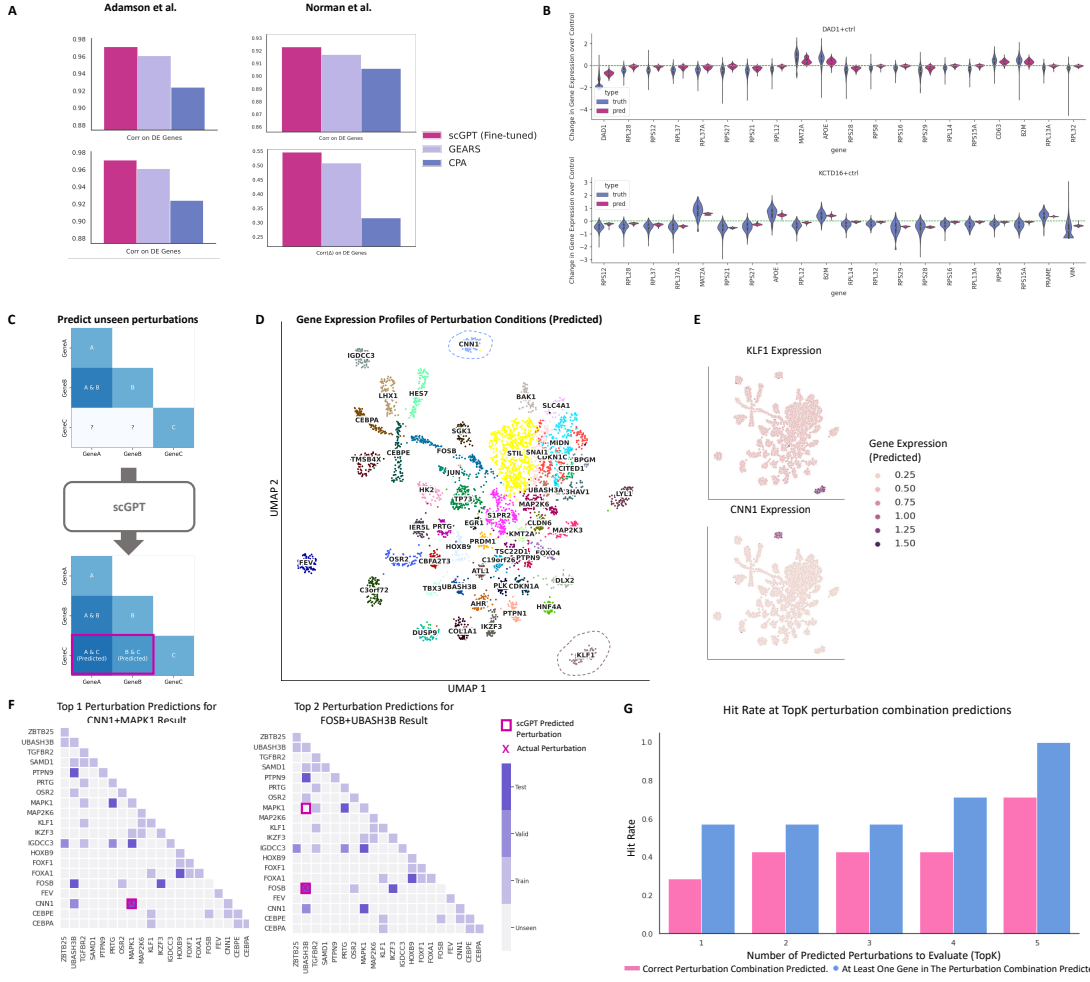


Figure 3: Prediction results for perturbation response and reverse perturbation. (A) Comparison between scGPT and other perturbation prediction methods. Two evaluation metrics are reported. (B) On the Adamson dataset, distribution of predicted and actual gene expression of top 20 differentially expressed genes. (C) Illustration diagram for predicting unseen perturbation responses using scGPT. (D) UMAP of predicted gene expression profiles of the perturbation conditions. The UMAP is colored by Leiden clusters and labeled by the dominant gene of each cluster. (E) Expression patterns of two selected perturbed genes over the UMAP of perturbation conditions. (F) Visualization of the possible perturbation combinations over the perturbation combination space of 20 genes. The grid is colored by experiment type (Train, Valid, Test, Unseen). All predicted perturbations are highlighted by squared boxes, and the actual source perturbation is marked by a cross. (G) Top 1-5 accuracy for correct and relevant predictions among the 7 test cases. The relevant predictions (blue) indicate at least one of the perturbed genes in the perturbation combination is found in the predictions.

204 aligns with expected outcomes of the CRIPRa Perturb-seq experiments in the Norman dataset.  
205 These dominant gene clusters demonstrate the capability of scGPT to uncover associations be-  
206 tween perturbation combinations, providing insights into their combined effects on gene expression  
207 profiles.

208 **In-silico Reverse Perturbation Prediction**

209 scGPT is also capable of predicting the source of genetic perturbation for a given resulting cell state,  
210 which we refer to as in-silico *reverse perturbation* prediction. An ideal prediction model conducting  
211 such reverse prediction can be used to infer important driving genes for lineage development or  
212 facilitate the discovery of potential therapeutic gene targets. A hypothetical example application  
213 of such capability could be to predict CRISPR target genes that influence cells to recover from  
214 a disease state. To showcase the effectiveness of reverse perturbation prediction, we utilized a  
215 subset of the Norman dataset focusing on perturbations involving 20 genes (Figure 3F). This  
216 combinatorial space consists of a total of 210 one-gene or two-gene perturbation combinations.  
217 We fine-tuned scGPT using 39 (19%) known perturbations (the train group in Figure 3F). We  
218 then tested the model on queries of unseen perturbed cell states, and scGPT successfully predicted  
219 the source of perturbations that would generate the observed results. Specifically, after ranking  
220 the top predictions for seven test examples, we found that scGPT accurately retrieved the actual  
221 source perturbations. For example, scGPT ranked the correct perturbation of *CNN1+MAPK1* as  
222 the top prediction for one test example, and the correct perturbation of *FOSB+UBASH3B* was  
223 ranked as the second prediction for another case (Figure 3F). Overall, scGPT identified 71.4%  
224 correct perturbations (5/7 test cases) within the top 5 predictions (the red bars in Figure 3G). We  
225 envision these predictions can be used for planning perturbation experiments by maximizing the  
226 possibility of deriving target cell states. Compared to random tryouts, which would on average  
227 require 105.5 attempts out of the 210 possible perturbations in this subset, finding the correct  
228 source of genetic change within 5 attempts represents a 95.2% speedup. The reverse perturbation  
229 predictions generated by scGPT offer a valuable tool for accelerating the discovery of important  
230 genetic drivers and optimizing perturbation experiments.

231 **2.4 scGPT enables accurate multi-batch and multi-omics integration**

232 **Multi-Batch scRNA-seq Integration**

233 Integrating multiple scRNA-seq data from different batches poses unique challenges in simultane-  
234 ously preserving the biological variance of integrated datasets and removing technical batch effects.  
235 In our benchmarking experiments, we compared scGPT with three popular integration methods:  
236 scVI [41], Seurat [42], and Harmony [43]. The evaluation was conducted on three integration  
237 datasets, namely the COVID-19 (18 batches) [13], PBMC 10K (2 batches) [44], and Perirhinal  
238 Cortex (2 batches) [45]. In the PBMC 10K dataset, scGPT stands out as the only method that  
239 successfully separates all the cell types. The other methods struggle with accurately distinguishing  
240 CD14+ Monocytes and CD8 T cells from other cell types (Figure 4A). This superior integra-  
241 tion performance of scGPT is further supported by its high biological conservation score, with an  
242 *AvgBIO* score of 0.821, which is 5-10% higher than the compared methods. The *AvgBIO* score  
243 aggregates three cell type clustering metrics *NMI<sub>cell</sub>*, *ARI<sub>cell</sub>*, and *ASW<sub>cell</sub>*, as detailed in Sup-  
244 plementary Online Methods S.5. Notably, scGPT also demonstrates a considerable performance  
245 for integrating PBMC 10K dataset even without fine-tuning (Supplementary Figure S5), high-  
246 lighting the generalizability of the pretraining. In the context of the Perirhinal Cortex dataset,  
247 scGPT remains competitive against all other methodologies (Supplementary Figure S6C). This

248 finding highlights the transferability and robustness of the features learned from the whole-human  
249 dataset, even when applied to specific organs/tissues such as the brain. Furthermore, in Supple-  
250 mentary Figure S6, scGPT consistently achieves competitive scores across all integration metrics  
251 and demonstrates strong conservation of biological signals. In terms of overall performance, con-  
252 sidering both biological conservation and batch correction, scGPT ranks at the top (See detailed  
253 metrics in Supplementary Table S2 and Supplementary Figure S7). Additionally, we have de-  
254 veloped strategies to accelerate the fine-tuning process for the integration task, including freezing  
255 specific model layers and excluding genes with no expression, while maintaining comparable results  
256 to our original approach (Supplementary Note S.3).

257 **Single-Cell Multi-Omic Integration**

258 Single-cell multi-omic (scMultiomic) data, which combines multiple views of genetic regulation such  
259 as epigenetic, transcriptomic, and translation activities, presents a unique challenge in aggregating  
260 cell representations while preserving biological signals [9, 10]. scGPT addresses this challenge by  
261 effectively extracting integrated cell embeddings across different omics. In the case of the 10X  
262 Multiome PBMC dataset [47], which includes joint gene expression and chromatin accessibility  
263 measurements, we compared scGPT with two state-of-the-art methods, scGLUE [14] and Seurat  
264 v4 [46], in terms of cell type integration performance. As depicted in Figure 4B, scGPT stands  
265 out as the only method that successfully generates a distinct cluster for CD8 Naive cells, while the  
266 other two methods fail to do so. Next, we tested scGPT on the paired gene expression and protein  
267 abundance dataset BMMC [48] as illustrated in Figure 4C. This dataset contains additional com-  
268 plexity from the large data size (90 thousand cells), multiple batches (12 donors), and fine-grained  
269 subgroup annotations (48 cell types). scGPT presented more defined cluster structures compared  
270 to Seurat v4, with a 9% improvement in the *AvgBIO* score. Notably, scGPT was able to sep-  
271 arate CD4+ T naive and CD4+ T activated cells as two distinct clusters. It also teased apart  
272 integrinB7+ activated CD4+ T cells from other CD4+ T cells, which further endorsed the model’s  
273 ability to capture the subtle differences between immune cell subgroups. Overall, scGPT demon-  
274 strates superior cell-type clustering performance in the paired data setting and exhibits robustness  
275 across diverse biological conservation metrics benchmarked (Figure 4D and Supplementary Table  
276 S3).

277 scGPT excels in integrating multi-modal batches from mosaic scMultiomic data through joint  
278 representation learning. In the mosaic data integration setting, sequenced samples share some, but  
279 not all, data modalities, posing a challenge for integration methods. To showcase the capabilities  
280 of scGPT in this context, we utilized the ASAP human PBMC dataset [49] as an example. This  
281 dataset consists of four sequencing batches with three data modalities: gene expression and protein  
282 abundance data from CITE-seq in the first two batches, and chromatin accessibility and protein  
283 abundance measurements from ASAP-seq in the second two batches. In the benchmark experiment  
284 with scMoMat[15], scGPT demonstrates superior batch correction performance as shown in Figure  
285 4D, especially in the rarer cell groups B, Myeloid, and NK cells. In comparison, scMoMat produced  
286 two distinct clusters for each cell type corresponding to the first two and second two batches,  
287 indicating failure to learn a joint representation. scGPT achieves a higher overall batch correction  
288 score *AvgBATCH* of 0.951 compared to scMoMat (*AvgBATCH* = 0.916). scGPT’s biological  
289 conservation metrics also compare favorably to scMoMat’s, which further indicates the robustness  
290 of multi-modal batch correction without interfering with the biological signals (Figure 4D and  
291 Supplementary Table S3).

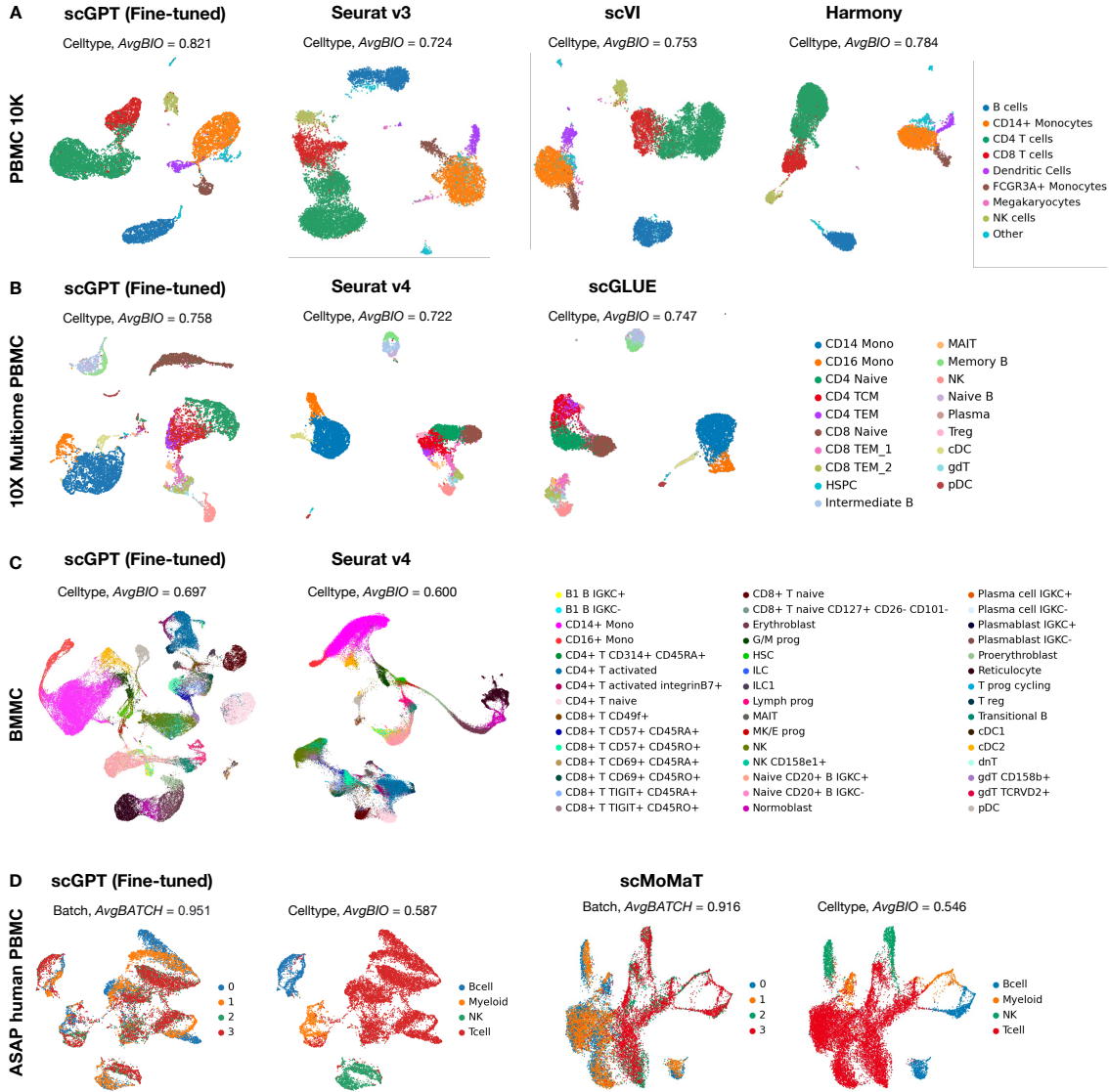


Figure 4: (A) Benchmark of the fine-tuned scGPT on the PBMC 10K dataset for cell type clustering task. The UMAP plot of learned cell embeddings was colored by *cell types*. (B) Benchmark of the fine-tuned scGPT model with scGLUE[14] and Seurat v4[46] on the 10x Multiome PBMC [47] dataset (paired RNA+ATAC data) for cell type clustering task. (C) Benchmark of the fine-tuned scGPT model with Seurat v4[46] on the BMMC [48] dataset (paired RNA+Protein data) for cell type clustering task. (D) Benchmark of scGPT with scMoMat[15] on the ASAP PBMC [49] dataset (mosaic RNA+ATAC+Protein data) for batch correction and cell type clustering tasks. The UMAP plots of learned gene embeddings were colored by *sequencing batches* (left) and *cell types* (right).

## 292 2.5 scGPT uncovers gene regulatory networks for specific cell states and 293 perturbation conditions

294 The interactivity between transcription factors, cofactors, enhancers, and target genes underlying a  
295 Gene Regulatory Network (GRN) mediates important biological processes. Existing GRN inference  
296 methods often rely on correlation in static gene expression or pseudo-time estimates as a proxy for  
297 causal graphs [50]. scGPT, optimized by generative modelling of gene expression, implicitly encodes  
298 such relationships in its gene embeddings as well as attention maps. The gene embeddings construct  
299 a similarity network that entails gene-gene interactions on the dataset level. The attention maps  
300 further capture the unique gene network activation patterns across different cell states. In this  
301 study, we validate the gene network extracted by scGPT against known biology and explore its  
302 applicability to gene program discovery.

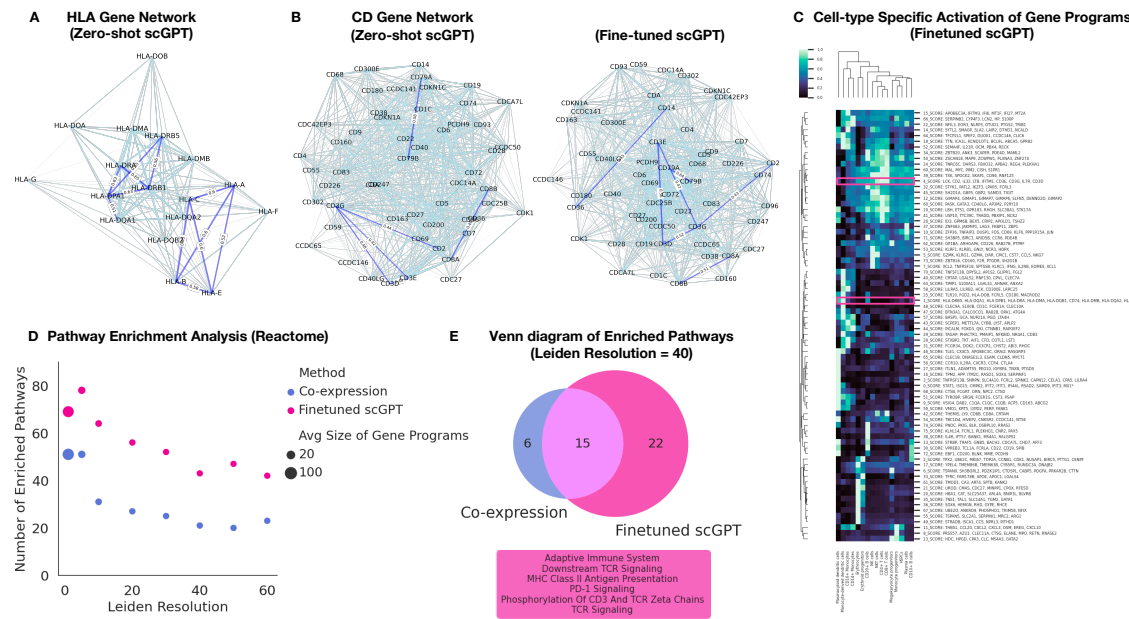


Figure 5: (A) HLA gene network from zero-shot scGPT. (B) CD gene network from the zero-shot (i.e., pre-trained) and fine-tuned scGPT on the Immune Human dataset. (C) Cell-type specific activation among scGPT-extracted gene programs in the Immune Human dataset. (D) Pathway enrichment analysis of the gene programs extracted by scGPT and co-expression network in the Immune Human dataset. The number of enriched pathways from scGPT’s gene programs was compared with the co-expression method at different Leiden resolutions. (E) Venn diagram to compare the overlap and differences between the enriched pathways identified by co-expression versus scGPT. Some example pathways unique to scGPT and specific to the adaptive immune functions are highlighted in the text box.

303 scGPT demonstrates its ability to group functionally related genes and differentiate functionally  
304 distinct genes via the learned gene token embeddings. In Figure 5A, we conducted a sanity check  
305 by visualizing the similarity network of the human leukocyte antigen (HLA) proteins using the  
306 pre-trained gene embeddings from the pre-trained scGPT model. In this zero-shot setting, the  
307 scGPT model successfully highlights two clusters corresponding to the well-characterized HLA  
308 classes: HLA class I and HLA class II genes. These classes encode antigen-presenting proteins  
309 that play different roles in immune contexts. For example, HLA class I proteins (such as *HLA-A*,  
310 -*C*, and -*E*) are recognized by CD8+ T cells and mediate cytotoxic effects, while HLA class II

311 proteins (such as HLA-DR, -DP, and -DQ) are recognized by CD4+ T cells and trigger broader  
312 helper functions [51]. In addition, we fine-tuned the scGPT model on the Immune Human dataset  
313 and explored the CD gene network specific to the immune cell types present in this dataset. We  
314 employed the same fine-tuning strategy as used for the integration task (Online Methods 4.5) for  
315 the purpose of GRN analysis. The pre-trained scGPT model successfully identifies the group of  
316 genes (*CD3E*, *D*, and *G*) encoding the T3 complex for T-cell activation, as well as *CD79A* and  
317 *CD79B* for B-cell signaling, and *CD8A* and *CD8B* as co-receptors for HLA class I molecules [52]  
318 (Figure 5B). Furthermore, the fine-tuned scGPT model highlights the connection between *CD36*  
319 and *CD14*, which serve as markers for monocytes and macrophages (Figure 5B). These findings  
320 demonstrate scGPT’s ability to generalize the knowledge learned during pre-training and extract  
321 information relevant to specific tissues or cell types after fine-tuning.

322 scGPT is able to uncover meaningful gene programs that exhibit cell-type specific activation  
323 via purely unsupervised pretraining and fine-tuning. At the inference stage, gene programs are  
324 subsequently selected and clustered using the gene embeddings from scGPT (Online Methods 4.5).  
325 In Figure 5C, we visualized the gene programs extracted by the fine-tuned scGPT model on the  
326 highly variable genes in the Immune Human dataset [53], and their expression in different cell types.  
327 We observed that a set of HLA class II genes was identified as group 1. Similarly, the CD3 genes  
328 involved in the T3 complex were identified as group 4, with the highest expression present in T  
329 cells. These findings confirm that scGPT’s inferred gene programs capture biologically meaningful  
330 functional groups.

331 In order to systematically validate the extracted gene programs, we performed pathway enrichment  
332 analysis against the Reactome database [54] and identified high-confidence “pathway hits”  
333 using stringent multiple-testing correction [55] (Online Methods 4.7). In Figure 5D, we compare  
334 the results obtained from scGPT with those from the co-expression network. Notably, scGPT  
335 consistently demonstrates a significantly higher number of enriched pathways across all clustering  
336 resolutions. Furthermore, we examined the similarities and differences in the identified pathways  
337 between scGPT and the co-expression network, as depicted in Figure 5E. Both methods identi-  
338 fied 15 common pathways, including those associated with the cell cycle and the immune system.  
339 However, scGPT uniquely identified additional 22 pathways, out of which 14 were immune-related.  
340 Notably, scGPT specifically highlighted pathways related to the adaptive immune system, T-cell  
341 receptor (TCR) signaling, PD-1 signaling, and MHC II presentation, which were not captured by  
342 the co-expression network. This is concordant with the fact that adaptive immune populations  
343 exist in the fine-tuning datasets. These findings demonstrate scGPT’s superior ability to cap-  
344 ture intricate gene-gene connections and unravel specific mechanisms within a broader biological  
345 context. The detailed list of enriched pathways is provided in Supplementary Table S4.

346 In addition to dataset-level gene network inference using gene embeddings, scGPT’s attention  
347 mechanism enables it to capture gene-gene interactions at the single-cell level. scGPT extracts cell-  
348 state-specific network activations by aggregating single-cell signals from the attention maps. This  
349 provides insights into the context-specific gene regulatory interactions within individual cells, which  
350 may vary across different cell states and conditions. For example, in a perturbation experiment,  
351 scGPT examines the changes in gene network activation pre- and post-perturbation to infer which  
352 genes are most influenced by each perturbed gene (Figure 6A and Online Methods 4.5). In the  
353 Adamson CRISPR interference dataset [36], scGPT identified the top 20 genes most influenced by  
354 *DDIT3* transcription factor repression, which are all found to be signaling targets of *DDIT3* in  
355 the Chip-Atlas database [56] (Figure 6B). Moreover, scGPT captured distinct pathway activation  
356 patterns among the top 100 most influenced genes by *DDIT3* in the control versus *DDIT3*-knockout  
357 settings. Notably, the ATF6 pathway identified in *DDIT3*-knockout setting is known to mediate  
358 unfolded protein response and regulates cell apoptosis [57, 58]. Similarly, in the case of *BHLHE40*  
359 repression, 19 out of the top 20 most influenced genes are found to be ChIP-seq predicted targets of

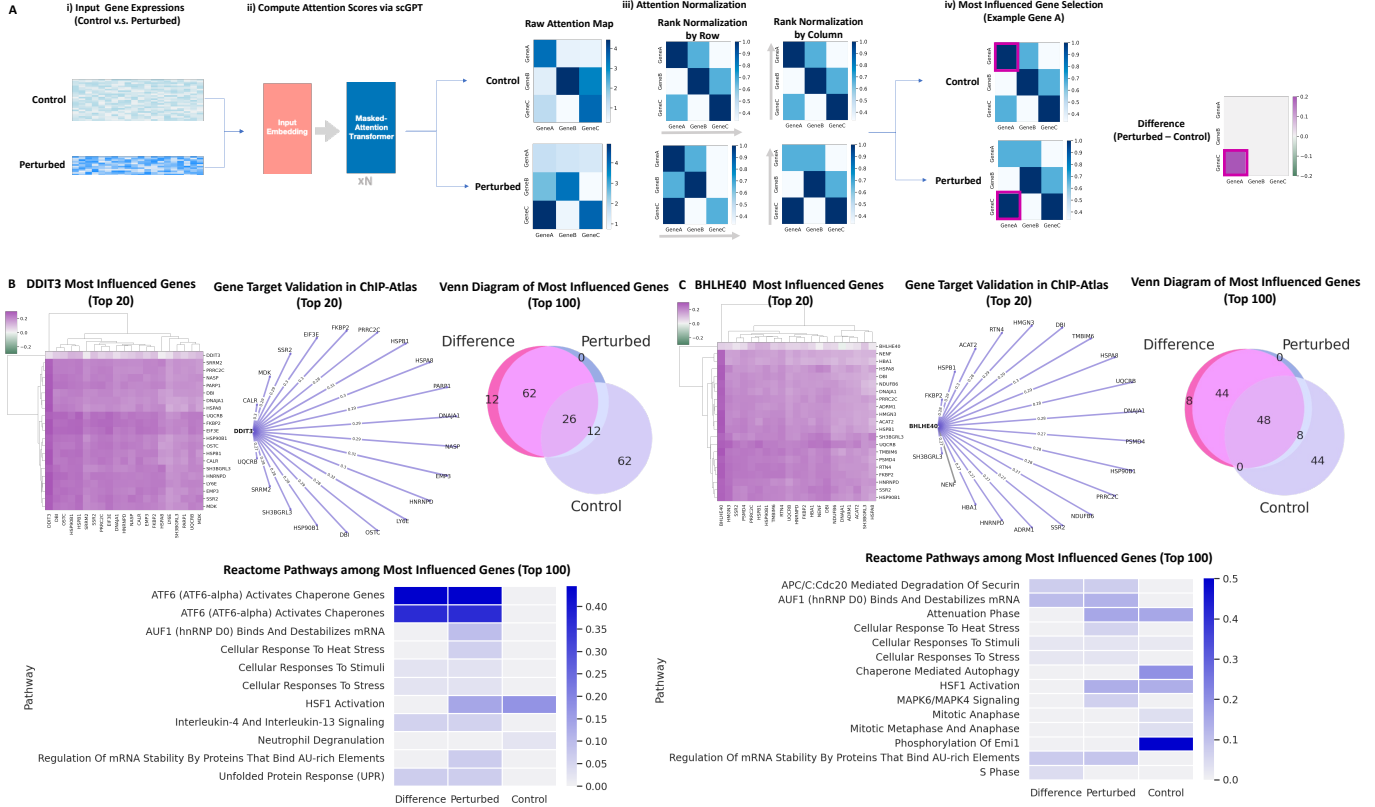


Figure 6: (A) Attention-based GRN discovery workflow for perturbation data. Attention scores in control and perturbed cell states are obtained and ranked by row and column consecutively. Most influenced genes in *Control*, *Perturbed*, and the *Difference* settings are selected accordingly. (B) GRN analysis for DDIT3 transcription factor repression. The gene connectivity heatmap presents post-perturbation changes in the network of the top 20 genes most influenced by DDIT3 repression. The gene target network graph showcases the top 20 genes validated in the CHIP-Atlas database, with ChIP-seq predicted targets highlighted in purple. The Venn diagram compares the overlaps and differences among the top 100 most influenced gene sets identified in three selection settings (i.e., *Control*, *Perturbed*, and post-perturbation *Difference*). The pathway heatmap showcases the difference in Reactome pathways identified from the top 100 most influenced genes across these three selection settings. The color indicates how strong each pathway is represented by the percentage of gene overlap. (C) GRN analysis for BHLHE40 transcription factor repression, visualized in a similar manner.

360 this transcription factor (Figure 6C). The pathway activation profile highlighting DNA synthesis  
361 and mitosis reflects the role of *BHLHE40* in cell cycle regulation [59]. These attention-based  
362 findings further validated scGPT’s learned gene network on a cell-state level, providing additional  
363 interpretability to the model’s learned biology.

364 These aforementioned results showcase the potential of scGPT for exploring gene-gene interactions  
365 in a general setting and for specific cell types and perturbation conditions. More specifically,  
366 we demonstrate its ability to perform unsupervised gene program discovery on new datasets that  
367 disentangle fine-grained biological mechanisms. The attention map further provides a prediction-  
368 based importance ranking approach that identifies cell-state-specific gene targets taking part in  
369 dynamic processes.

## 370 2.6 Analyzing the transfer learning of pretrained knowledge: the scaling 371 law and in-context effects

372 In previous sections, scGPT has demonstrated great potential via fine-tuning in a transfer learning  
373 manner. We further confirmed the benefits of using the foundation model by comparing it with  
374 similar transformer models trained for each downstream task from scratch without pretraining  
375 (denoted as scGPT (from-scratch)). The results are listed in Supplementary Tables S1, S2, S3,  
376 where the fine-tuned scGPT consistently showcases performance gain for tasks such as integration  
377 and cell type annotation. Given the observed contributions of the foundation model for downstream  
378 tasks, we are further interested in exploring the factors influencing the transfer learning process.

379 Firstly, we delve into the relationship between *pre-training data size* and the performance of  
380 fine-tuned models. We pre-trained a series of scGPT models of the same number of parameters  
381 but using different sizes of data, from 30K to 33M sequenced normal human cells. Figure 2D and  
382 E illustrate the actual performance of fine-tuning for the cell type annotation task using these  
383 various pre-trained models. We observed the performance of fine-tuned models improved as the  
384 size of the pre-training data increased. These results confirm the *scaling law*, suggesting that  
385 larger pre-training data size leads to better pre-trained embeddings and improved performance  
386 on downstream tasks. On the other hand, we acknowledge the importance of considering model  
387 size alongside data size. Previous research has shown a correlation between optimal model size  
388 and data size, as discussed [60]. While the scaling law trend in Figure 2E may appear to reach a  
389 saturation point after the 3M data size, we hypothesize that increasing the model size would lead  
390 to improved performance even at 33M data size and beyond. We leave the exploration of larger  
391 model sizes to future work.

392 Notably, our findings also align with the scaling law reported in natural language models  
393 [60], highlighting the significant role of data size in model performance. The crucial role of pre-  
394 training data size in fine-tuning results points to a promising future for pretrained models in the  
395 single-cell domain. As larger and more diverse datasets become available, we can anticipate further  
396 improvements in model performance, advancing our understanding of cellular processes. Pretrained  
397 models will continue to expand their capabilities, facilitating breakthroughs in single-cell research  
398 and unlocking new discoveries in cellular biology.

399 The second factor we explored is the influence of context-specific pre-training. Here, an *in-*  
400 *context usage* refers to an scGPT model that is pre-trained on specific cell types and then fine-tuned  
401 for a downstream task on similar cell types. To explore the influence of this factor, we pre-trained  
402 seven organ-specific models on the normal human cells from individual major organs (Figure 1D)  
403 and another model for pan-cancer cells. We verified the efficacy of the pretraining by visualizing  
404 the cell embeddings of the pre-training data: the pan-cancer model cell embeddings accurately

405 separate different cancer types (Supplementary Figure S2). The organ-specific models are able to  
406 reveal cell heterogeneity of corresponding organs (Supplementary Figure S3). Interestingly, since  
407 the training data per organ were collected in different sizes, the organ-specific pretrained models  
408 again confirmed the scaling law: models pre-trained on larger data ( $> 800,000$  cells) exhibited  
409 cell embeddings better separating the cell types, as shown in Supplementary Figure S3. Next,  
410 removing the influence of data sizes, we used the rest five organ-specific models (i.e., the brain,  
411 blood, heart, lung, and kidney models) with sufficient training data for the analysis of in-context  
412 effects. The COVID-19 dataset serves as an ideal task for this investigation, as it comprises diverse  
413 cellular compositions. Our analysis reveals a clear correlation between the relevance of the model's  
414 context in pre-training and its subsequent performance for integrating the COVID-19 dataset  
415 (Supplementary Figure S8). The top performers in data integration tasks were models pretrained  
416 on whole-human, blood, and lung datasets, which closely aligned with the cell types present in the  
417 COVID-19 dataset. Notably, even a brain pre-trained model, despite being trained on a substantial  
418 dataset of 13 million cells, trailed in performance by 8% compared to the blood pre-trained model  
419 with similar dataset size. This emphasizes the importance of aligning the cellular context in pre-  
420 training with the target dataset for superior results in downstream tasks. While considering the  
421 cellular context is essential, the whole-human pre-trained model emerges as a versatile and reliable  
422 option for a wide range of applications.

423 In summary, our analysis demonstrates the contribution of pretrained knowledge to downstream  
424 analysis, the scaling law between pre-training data size and fine-tuning results, and the impact of  
425 context-specific pre-training. These findings highlight the potential of pretrained models to advance  
426 our understanding of cellular biology and pave the way for future discoveries.

### 427 3 Discussion

428 We introduce scGPT, a pioneering generative pretrained foundation model that harnesses the  
429 power of pre-trained transformers on a vast amount of single-cell data. Building upon the success  
430 of self-supervised pre-training in language models like chatGPT and GPT4 [18, 19], we adopted  
431 a similar approach in the single-cell domain to unravel complex biological interactions. The use  
432 of transformers in scGPT enables the simultaneous learning of gene and cell embeddings, which  
433 facilitates the modeling of various aspects of cellular processes. By leveraging the attention mech-  
434 anism of transformers, scGPT captures gene-to-gene interactions at the single-cell level, providing  
435 an additional layer of interpretability.

436 We demonstrated the benefits of pre-training with comprehensive experiments in both zero-shot  
437 and fine-tuning settings. The pre-trained model itself is a universal feature extractor. It showcases  
438 strong capabilities of extrapolating to unseen datasets, presenting meaningful cell clustering in zero-  
439 shot experiments. In addition, the learned gene networks in scGPT exhibit strong alignment with  
440 known functional connections. The model's ability to accurately capture gene-gene interactions  
441 and reflect known biological knowledge provides confidence in its capacity to uncover meaningful  
442 insights in single-cell biology. Furthermore, the pre-trained model's knowledge can be transferred  
443 to multiple downstream tasks through fine-tuning. In tasks such as cell type annotation, multi-  
444 batch and multi-omic integration, the fine-tuned scGPT model consistently outperforms models  
445 trained from scratch. This demonstrates the valuable contribution of the pre-trained model to  
446 downstream tasks, enabling more accurate and biologically meaningful analyses. Overall, our  
447 experiments highlight the efficacy of pre-training in scGPT, showcasing its ability to generalize,  
448 capture gene networks, and improve performance in downstream tasks through transfer learning.

449 For future directions, we plan to pre-train on a larger-scale dataset with more diversity, in-

450       cluding multi-omic data, spatial omics, and various diseased conditions. It is also interesting to  
451       incorporate perturbation and temporal data in the pre-training stage, enabling the model to learn  
452       causal relationships and infer how genes and cells respond to changes over time. More importantly,  
453       we would like to validate the pre-trained model on a wider range of biologically meaningful tasks  
454       to understand and interpret what the pre-trained model has learned. We also aim to explore  
455       in-context instruction learning for single-cell data. This involves developing techniques that al-  
456       low the pre-trained model to understand and adapt to different tasks and contexts in a zero-shot  
457       setting, without the need for fine-tuning. By enabling scGPT to grasp the nuances and specific  
458       requirements of different analyses, we can enhance its usability and applicability in a wide range of  
459       research scenarios. We envision that the pre-training paradigm be readily integrated into single-  
460       cell research, and serve as a foundation to leverage the existing knowledge from the exponentially  
461       growing cell atlases for new discoveries.

## 462       4 Methods

### 463       4.1 Input embeddings

464       The single-cell sequencing data is processed into a cell-by-gene matrix,  $\mathbf{X} \in \mathbb{R}^{N \times G}$ , where each  
465       element  $X_{i,j} \in \mathbb{R}^+$  represents the read count of an RNA molecule in the case of scRNA-seq or a  
466       peak region in the case of scATAC-seq. Specifically, in scRNA-seq, the element denotes the RNA  
467       abundance for gene  $j \in 0, 1, \dots, G$  in cell  $i \in 0, 1, \dots, N$ . In subsequent sections, we will refer to  
468       this matrix as the raw matrix. The input to scGPT consists of three main components: (1) gene  
469       (or peak) tokens, (2) expression values, and (3) condition tokens. For each modelling task, the  
470       gene tokens and expression values are pre-processed from the raw count matrix  $\mathbf{X}$  accordingly.

471       **Gene Tokens** In the scGPT framework, each gene is considered the smallest unit of information,  
472       analogous to a word in natural language generation (NLG). We therefore use gene names as tokens,  
473       and assign each gene  $g_j$  a unique integer identifier  $id(g_j)$ . These identifiers form the vocabulary  
474       of tokens used in scGPT. This approach offers great flexibility to harmonize multiple studies with  
475       different gene sets (i.e., generated by distinct sequencing technologies or pre-processing pipelines).  
476       Specifically, different sets of gene tokens can be integrated into a common vocabulary by taking the  
477       union set of all genes across studies. Additionally, we incorporate special tokens in the vocabulary,  
478       such as  $<cls>$  for aggregating all genes into a cell representation, and  $<pad>$  for padding the  
479       input to a fixed length. Conceptually, we draw parallels between gene tokens and word tokens in  
480       NLG. The input gene tokens of each cell  $i$  are hence represented by a vector  $\mathbf{t}_g^{(i)} \in \mathbb{N}^M$ :

$$\mathbf{t}_g^{(i)} = [id(g_1^{(i)}), id(g_2^{(i)}), \dots, id(g_M^{(i)})], \quad (1)$$

481       where  $M$  is a pre-defined maximum input length.

482       **Expression Values** The gene expression matrix  $X$  requires additional processing before being  
483       used as input for modelling. A fundamental challenge in gene expression modelling is the vari-  
484       ability in absolute magnitudes across different sequencing protocols [61]. Variations in sequencing  
485       depths and the presence of sparsely expressed genes result in significant differences in data scales  
486       among different batches of sequencing samples. These differences are not easily mitigated with  
487       common preprocessing techniques such as transcripts per million (TPM) normalization and  $\log_{10}$   
488       transformation [62]. Even after these transformations, the same absolute value can convey different

489 “semantic” meanings across sequencing batches. To address this scale difference, we propose the  
 490 ***value binning*** technique to convert all expression counts into relative values. For each non-zero  
 491 expression count in each cell, we calculate the raw absolute values and divide them into  $B$  consec-  
 492 utive intervals  $[b_k, b_{k+1}]$ , where  $k \in \{1, 2, \dots, B\}$ . Each interval represents an equal portion of all  
 493 expressed genes ( $1/B$ ). It is important to note that a new set of bin edges is computed for each  
 494 cell, so the interval edges  $b_k$  may vary among cells. The binned expression value  $x_j^{(i)}$  for cell  $i$  is  
 495 defined as:

$$x_j^{(i)} = \begin{cases} k, & \text{if } X_{i,j} > 0 \text{ and } X_{i,j} \in [b_k, b_{k+1}], \\ 0, & \text{if } X_{i,j} = 0. \end{cases} \quad (2)$$

496 Through this binning technique, the semantic meaning of  $x_j^{(i)}$  is consistent across cells from various  
 497 sequencing batches. For instance, a value of  $x_j^{(i)} = B$  consistently indicates the highest expression  
 498 among genes. Notably for fine-tuning tasks, we also performed  $\log 1p$  transformation and highly  
 499 variable gene selection [63] before the value binning step. To simplify the notation, we use  $X_{i,j}$  to  
 500 represent both the raw and preprocessed data matrices prior to binning. Therefore, the final input  
 501 vector of binned expression values for cell  $i$  is denoted as

$$\mathbf{x}^{(i)} = [x_1^{(i)}, x_2^{(i)}, \dots, x_M^{(i)}]. \quad (3)$$

502 **Condition Tokens** The condition tokens encompass diverse meta information associated with  
 503 individual genes, such as perturbation experiment alterations (indicated by perturbation tokens).  
 504 To represent position-wise condition tokens, we utilize an input vector that shares the same di-  
 505 mension as the input genes. This vector is denoted as:

$$\mathbf{t}_c^{(i)} = [t_{c,1}^{(i)}, t_{c,2}^{(i)}, \dots, t_{c,M}^{(i)}], \quad (4)$$

506 where  $t_{c,j}^{(i)}$  represents an integer index corresponding to a condition.

507 **Embedding layers** We utilize the conventional embedding layers<sup>1</sup>  $\mathbf{emb}_g$  and  $\mathbf{emb}_c$  for the gene  
 508 tokens and condition tokens, respectively, to facilitate the mapping of each token to a fixed-length  
 509 embedding vector of dimension  $D$ . We employ fully connected layers, denoted as  $\mathbf{emb}_x$ , for the  
 510 binned expression values to enhance expressivity. This choice enables the modelling of the ordinal  
 511 relation of gene expression values. Consequently, the final embedding  $\mathbf{h}^{(i)} \in \mathbb{R}^{M \times D}$  for cell  $i$  is  
 512 defined as,

$$\mathbf{h}^{(i)} = \mathbf{emb}_g(\mathbf{t}_g^{(i)}) + \mathbf{emb}_x(\mathbf{x}^{(i)}) + \mathbf{emb}_c(\mathbf{t}_c^{(i)}). \quad (5)$$

## 513 4.2 Cell and gene expression modelling by transformers

### 514 4.2.1 scGPT Transformer

515 We employ the self-attention transformer [27, 64] to encode the complete input embedding  $\mathbf{h}^{(i)}$   
 516 in equation 5. The self-attention mechanism operates on the sequence of  $M$  embedding vectors,

---

<sup>1</sup>pytorch embedding layer

517 making it particularly suitable for capturing interactions between genes. The output of the stacked  
 518 transformer blocks can be defined as follows:

$$\begin{aligned} \mathbf{h}_0^{(i)} &= \mathbf{h}^{(i)} \\ \mathbf{h}_l^{(i)} &= \text{transformer\_block}(\mathbf{h}_{l-1}^{(i)}) \quad \forall l \in [1, n] \end{aligned} \quad (6)$$

519 We utilize the resulting representation  $\mathbf{h}_n^{(i)} \in \mathbb{R}^{M,D}$  for both gene-level and cell-level tasks.  
 520 Gene-level fine-tuning objectives (Online Methods 4.4) are directly applied. Examples include the  
 521 gene expression prediction (GEP) objective and the perturbed expression prediction task (perturb-  
 522 GEP). For cell-level tasks, we first integrate  $\mathbf{h}_n^{(i)}$  into a cell embedding vector (Online Methods  
 523 4.2.2). An example would be the cell type assignment task, where the cell embeddings are used to  
 524 predict cell type labels by an added classifier in the CLS training objective.

525 The input dimension  $M$  can reach tens of thousands of genes, significantly exceeding the input  
 526 length of conventional transformers commonly used in NLG. To address this challenge and ensure  
 527 efficient self-attention mechanisms, we leverage the accelerated self-attention implementation by  
 528 Flash-Attention [65]. This implementation effectively enhances the model capacity and enables  
 529 the effective processing of large input dimensions. Although Flash-Attention was adopted, any  
 530 efficient transformers can be potentially utilized for scGPT as well, such as Transformers with  
 531 linear complexity (Lformer) [66] and Kernelized Self-Attention (KSA) [67].

#### 532 4.2.2 Cell representation

533 Each cell is analogous to a “sentence” composed of genes, and its representation  $\mathbf{h}_c^{(i)} \in \mathbb{R}^D$  is  
 534 obtained by aggregating the learned gene-level representations  $\mathbf{h}_n^{(i)}$ . Various pooling operations,  
 535 such as element-wise mean-pooling or weighted-pooling, can be readily employed in this context.  
 536 In this study, we opt to employ a special token  $<\text{cls}>$  for the cell representation, enabling the  
 537 model to learn the pooling operation within transformer blocks. The  $<\text{cls}>$  token is appended  
 538 to the beginning of the input tokens, and the final embedding at this position is extracted as the  
 539 cell representation. Consequently, the cell embedding  $\mathbf{h}_c^{(i)}$  can be extracted by the corresponding  
 540 row in the stacked final-layer embeddings  $\mathbf{h}_n^{(i)}[<\text{cls}>]$ , where the  $[<\text{cls}>]$  operation retrieves  
 541 the row at the index of the  $<\text{cls}>$  token position.

#### 542 4.2.3 Representation for batch and modality

543 We use additional sets of tokens to represent different sequencing batches and sequencing modalities  
 544 (genes from RNA-seq, peaks from ATAC-seq, etc.), specifically for the scRNA-seq and scMultiomic  
 545 integration tasks. This is similar to condition tokens introduced in Online Methods 4.1, and im-  
 546 plemented similarly using the standard embedding layers. The modality tokens  $\mathbf{t}_m^{(i)}$  are associated  
 547 with individual input features  $g_j$  (e.g., to indicate whether it is a gene, region or protein). The  
 548 batch tokens are on the cell level originally but can be propagated to all features of a single cell  
 549 as well. In other words, the same batch token  $t_b^{(i)}$  can be repeated up to the length  $M$  of input  
 550 features of single cell  $i$ :

$$\mathbf{t}_b^{(i)} = [t_{b,1}^{(i)}, t_{b,2}^{(i)}, \dots, t_{b,M}^{(i)}] = [t_b^{(i)}, t_b^{(i)}, \dots, t_b^{(i)}]. \quad (7)$$

551        The difference between the tokens described in Online Methods 4.1 and the batch and modal-  
552        ity tokens is that these embeddings of batch and modality tokens are not used as input to the  
553        transformer blocks. Instead, they are concatenated with the transformer output on either feature  
554        or cell level prior to entering specific fine-tuning objectives. This is to prevent the transformer  
555        from amplifying the attention within features of the same modalities while underestimating those  
556        of different modalities. Furthermore, knowing the modality and/or batch identities facilitates gene  
557        expression modelling in the downstream fine-tuning objectives. As the model learns to predict ex-  
558        pression values conditioned on modality and/or batch identities, such biases are implicitly removed  
559        from the gene and cell representations themselves. This serves as a technique to facilitate batch  
560        correction.

561        As an example, in the scMultiomic integration task, we concatenate the transformer output with  
562        the sum of batch and modality embeddings. This serves as input to the downstream fine-tuning  
563        objectives for expression modelling:

$$\mathbf{h}'^{(i)}_n = concat(\mathbf{h}^{(i)}_n, \mathbf{emb}_b(t_b^{(i)}) + \mathbf{emb}_m(t_m^{(i)})), \quad (8)$$

564        where  $\mathbf{emb}_b$  and  $\mathbf{emb}_m$  denote the batch and modality embedding layers respectively.  $\mathbf{h}^{(i)}_n$  denotes  
565        the output of the transformer layer (Online Methods 4.2.1).

566        Alternatively, in the scRNA-seq integration task, concatenation of batch embedding with the  
567        cell representation yields the following representation as input:

$$\mathbf{h}'^{(i)}_c = concat(\mathbf{h}^{(i)}_c, \mathbf{emb}_b(t_b^{(i)})), \quad (9)$$

568        where  $t_b^{(i)}$  denotes the batch identity of cell  $i$ .  $\mathbf{h}^{(i)}_c$  is the original cell representation in Online  
569        Methods 4.2.2.

## 570        4.3 Generative pre-training

### 571        4.3.1 Foundation model pre-training

572        The foundation model is designed to be a generalizable feature extractor that can benefit a diverse  
573        range of downstream tasks. The token vocabulary used in pre-training contains the entire set  
574        of genes in the human genome. The expression values were binned prior to model pre-training  
575        (Online Methods 4.1). To speed up the training, we restrict the input to only genes with non-  
576        zero expression for each input cell. To efficiently train the model to capture gene-gene relation  
577        and gene-cell relation, we introduce a new generative training strategy with specialized attention  
578        masks as described in the following section.

### 579        4.3.2 Attention mask for generative pre-training

580        Self-attention has been widely used to capture the co-occurrence patterns among tokens. In natural  
581        language processing, this has been achieved mainly in two ways: (1) masked token prediction used  
582        in transformer encoder models such as BERT [64] and Roberta [68], where randomly masked tokens  
583        in the input sequence are predicted in the model's output; (2) auto-regressive generation with  
584        sequential prediction in causal transformer decoder models such as the OpenAI GPT series [69, 70,  
585        71, 19]. The generative pre-training used in OpenAI GPT3 [71] and GPT4 [19] employs a unified

586 framework in which the model predicts the most likely next token from a “prompt” consisting  
587 of known input tokens. This framework offers great flexibility to be utilized in various natural  
588 language generation (NLG) applications and demonstrates new capabilities such as contextual  
589 awareness in zero-shot and fine-tuned settings [72]. We believe that generative training can be  
590 beneficial to single-cell models in a similar manner. Specifically, we are interested in two tasks: (1)  
591 generating unknown gene expression values based on known gene expression, i.e., generation by  
592 “gene prompts”, and (2) generating whole genome expression given an input cell type condition,  
593 i.e., generation by “cell prompts”.

594 Despite similar ideas of tokens and prompts, modelling genetic reads is inherently different  
595 from natural language due to the non-sequential nature of the data. Unlike words in a sentence,  
596 the order of genes within a cell is interchangeable, and there is no equivalent concept of the “next  
597 gene” to predict. This makes it challenging to apply the causal masking formulation from GPT  
598 models directly in single-cell data. To address this challenge, we developed a specialized attention  
599 masking mechanism for scGPT that defines the order of prediction based on attention scores.

600 The scGPT’s attention mask supports both gene-prompt and cell-prompt generations in a  
601 unified way. The binary attention mask is applied on the self-attention map in the transformer  
602 blocks. For an input  $\mathbf{h}_l^{(i)} \in \mathbb{R}^{M \times D}$  of  $M$  tokens (Online Methods 4.2.1), the transformer block  
603 will generate  $M$  query and key vectors to compute the attention map,  $\mathbf{A} \in \mathbb{R}^{M \times M}$ . The attention  
604 mask is of the same size  $M \times M$ . We visualize the attention mask in Supplementary Figure S1A,  
605 where queries are organized in rows and keys in columns. The token identity associated with each  
606 column of the mask is annotated at the bottom of the figure, namely  $<cls>$ , known genes, and  
607 unknown genes. Each token in the input embedding  $\mathbf{h}_l^{(i)}$  can be one of these three groups: (1)  
608 the reserved  $<cls>$  token for cell embedding (introduced in Online Methods 4.2.2), (2) known  
609 genes with token embeddings and expression value embeddings, and (3) unknown genes whose  
610 expression values are to be predicted. The rule of thumb for scGPT’s attention-masking is to only  
611 allow attention computation between embeddings of the “known genes” and the query gene itself.  
612 In each generation iteration, scGPT predicts the gene expression values of a new set of genes, and  
613 these genes in turn become the “known genes” in the next iteration for attention computation.  
614 This approach reflects the casual masking design with next token prediction in the conventional  
615 transformer decoders by making sequential predictions in the non-sequential single-cell data.

616 As illustrated in Supplementary Figure S1A, during training, we randomly pick a proportion of  
617 the genes as unknown so their expression values are omitted in the input. Attention is only applied  
618 between the known genes and the query unknown gene itself, but not onto the positions of other  
619 unknown genes. For example, the last gene to predict at position M has attention scores with the  
620 cell embedding, known genes, and itself only, but not the other unknown genes, as illustrated in the  
621 last row of the attention mask. The scGPT model predicts the expression for these unknown genes  
622 via the stacked transformer blocks with the masked attention map described above. The inference  
623 steps are illustrated in Supplementary Figure S1B. During the inference for cell-prompt generation,  
624 scGPT generates all genome-wide gene expression conditioned on the specific cell types. A trained  
625 cell embedding is inputted at the first position representing the cell type condition. The whole  
626 generation process of thousands of gene expression values is conducted in  $K$  iterative steps (i.e.,  
627  $K = 3$  steps in Supplementary Figure S1B). For example, in one iteration  $i \in \{1, 2, \dots, K\}$ , the  
628 attention masking mechanism allows attention with all predicted genes from previous 0 to  $i - 1$   
629 iterations. In each iteration, scGPT selects the top  $1/K$  genes from the unknown set with the  
630 highest prediction confidence to be included as known genes in the next iteration  $i + 1$ . Intuitively,  
631 this workflow streamlines the generation of gene expression in an auto-regressive manner, where  
632 gene expression values with highest prediction confidence are first generated and used to help  
633 subsequent rounds of generation. The gene-prompt generation works similarly in an iterative  
634 manner. The difference is that it starts with a set of known genes with observed expression values,

635 instead of a cell embedding.

636 The scGPT attention masking unifies the encoding process of known genes and the generation  
637 of unknown genes. It also stands as one of the first transformer schemes to conduct auto-regressive  
638 generation for non-sequential data.

639 **4.3.3 Learning objective**

640 We used a **gene expression prediction** objective to optimize the model to predict the expression  
641 values for unknown genes. Specifically, we employ a Multi-Layer Perceptron Network (MLP) to  
642 estimate the unknown expression values.

$$\mathcal{L} = \frac{1}{|\mathcal{U}_{unk}|} \sum_{j \in \mathcal{U}_{unk}} (\text{MLP}(\mathbf{h}_n^{(i)}) - x_j^{(i)})^2, \quad (10)$$

643 where  $\mathcal{U}_{unk}$  denotes the set of the output positions for unknown genes, and the  $x_j^{(i)}$  is the actual  
644 gene expression value to be predicted. The  $|\cdot|$  operation retrieves the number of elements of the  
645 set.

646 As mentioned in Online Methods 4.3.2, both gene-prompt and cell-prompt generations are  
647 supported. During training, these two modes are conducted consecutively. Among the input gene  
648 tokens of one given cell, a proportion of the genes are selected to be the “unknown” genes and their  
649 expression values are omitted. Firstly, in the gene-prompt step, the input to the model contains  
650 the  $<cls>$  token embedding, the known gene embeddings, and the unknown gene embeddings.  
651 The loss (Equation 10) is computed using the model’s output. Secondly, in the cell-prompt step,  
652 the output cell embedding (i.e.,  $\mathbf{h}_c^{(i)}$  in Online Methods 4.2.2) from the previous step is used to  
653 replace the embedding at the  $<cls>$  position. Other computations remain the same. Finally, the  
654 loss values of the two steps are added together and used to compute the gradients to optimize the  
655 model parameters.

656 **4.4 Fine-tuning objectives**

657 scGPT leverages various fine-tuning objectives to facilitate the learning of biologically valid repre-  
658 sentations of cells and genes, as well as for regularization purposes such as batch correction.

659 **Gene Expression Prediction (GEP)** To encourage the learning of gene-gene interactions,  
660 scGPT incorporates gene expression prediction. This fine-tuning objective works similarly to the  
661 objective in pre-training (Online Methods 4.3.3), but applies to masked positions instead. To be  
662 specific, for each input cell, a subset of gene tokens and their corresponding expression values  
663  $\mathbf{x}^{(i)}$  are randomly masked. scGPT is optimized to accurately predict the expression values at  
664 the masked positions. This fine-tuning objective benefits the model in effectively encoding co-  
665 expression among the genes in the dataset. The objective minimizes the mean squared error at  
666 the masked positions, denoted as  $\mathcal{M}_{mask}$ . The GEP works as follows,

$$\begin{aligned} \tilde{\mathbf{x}}^{(i)} &= \text{MLP}(\mathbf{h}_n^{(i)}), \\ \mathcal{L}_{GEP} &= \frac{1}{|\mathcal{M}_{mask}|} \sum_{j \in \mathcal{M}_{mask}} (\tilde{x}_j^{(i)} - x_j^{(i)})^2. \end{aligned} \quad (11)$$

667 Here,  $\tilde{\mathbf{x}}^{(i)} \in \mathbb{N}^M$  represents the row of expression estimates for cell  $i$ . Notably, if sequencing  
 668 batches or modality conditions are provided, we use  $\mathbf{h}_n'^{(i)}$  from Equation 8 instead of  $\mathbf{h}_n^{(i)}$ .

669 GEP presents a general self-supervised fine-tuning objective, which aims to forecast gene ex-  
 670 pression values. In certain downstream tasks, such as perturbation prediction, the model is re-  
 671 quired to predict perturbed gene expression values instead of the original values. We refer to this  
 672 variation as **perturb-GEP**. We maintain the MLP estimator in equation 11, but utilize the post-  
 673 perturbation gene expression as the target  $x_j^{(i)}$ . In perturb-GEP, the model is supposed to predict  
 674 the post-perturbation expression of all input genes.

675 **Gene Expression Prediction for Cell Modelling (GEPC)** This fine-tuning objective op-  
 676 erates similarly to GEP, but predicts gene expression values based on the cell representation  $\mathbf{h}_c^{(i)}$   
 677 to explicitly facilitate cell representation learning. For each gene  $j$  in an input cell  $i$ , we create a  
 678 query vector  $\mathbf{q}_j$  and utilize the parameterized inner product of  $\mathbf{q}_j$  and the cell representation  $\mathbf{h}_c^{(i)}$   
 679 as the predicted expression value.

$$\begin{aligned} \mathbf{q}_j &= \text{MLP}(\text{emb}_g(\mathbf{t}_g^{(i)})), \\ \tilde{x}_j^{(i)} &= \mathbf{q}_j \cdot \mathbf{W} \mathbf{h}_c^{(i)}, \\ \mathcal{L}_{GEPC} &= \frac{1}{|\mathcal{M}_{mask}|} \sum_{j \in \mathcal{M}_{mask}} (\tilde{x}_j^{(i)} - x_j^{(i)})^2. \end{aligned} \quad (12)$$

680 GEP inherits the gene token embedding,  $\text{emb}_g(\mathbf{t}_g^{(i)})$ , from equation 5. In integration tasks,  
 681 we utilize  $\mathbf{h}_c'^{(i)}$  from Equation 9 instead of  $\mathbf{h}_c^{(i)}$ . In our experiments, we observed that combining  
 682 GEP and GEPC leads to significantly improved performance compared to using either method  
 683 individually.

684 **Elastic Cell Similarity (ECS)** This fine-tuning objective enhances cell representations through  
 685 the utilization of a similarity learning loss [73]:

$$\mathcal{L}_{ECS} = -(\text{sim}(\mathbf{h}_c^{(i)}, \mathbf{h}_c^{(i')}) - \beta)^2, \quad (13)$$

686 where **sim** represents the cosine similarity function, while  $i$  and  $i'$  refer to two cells within the mini-  
 687 batch. Additionally,  $\beta$  denotes a predefined threshold. The underlying idea behind this approach is  
 688 to enhance the similarity between pairs exhibiting cosine similarity values above  $\beta$ , thereby making  
 689 them even more similar. Conversely, dissimilar pairs are encouraged to be further apart.

690 **Domain Adaptation via Reverse Back-Propagation (DAR)** Cell representation learning  
 691 is hindered by the presence of batch effects, which result from non-biological batch differences

692 introduced by sequencing technologies [74, 75]. To mitigate this problem, we employ a distinct  
693 multi-layer perceptron (MLP) classifier to predict the sequencing batch associated with each input  
694 cell, and modify the back-propagation process by reversing the gradients within the model. This  
695 approach leverages insights from the robust domain adaptation method proposed by Ganin and  
696 Lempitsky [76].

697 **Cell Type Classification (CLS)** This fine-tuning objective is designed to leverage the learned  
698 cell representations to annotate single cells. We use a separate MLP classifier to predict the cell  
699 types from their cell representations  $h_c^{(i)}$ . This fine-tuning objective is optimized with the cross-  
700 entropy loss  $ce$  between the predicted cell type probabilities and ground-truth labels.

## 701 4.5 Fine-tuning on downstream tasks

702 **Cell type annotation** For the cell type annotation task, we fine-tuned the model on a reference  
703 set with ground-truth labels, and validated the annotation performance on a held-out query set.  
704 The common set of gene tokens between the pre-trained foundation model and the reference set was  
705 retained. The gene expression values were normalized, log-transformed, and binned prior to model  
706 fine-tuning. All pre-trained model weights were used to initialize the fine-tuned model, except for  
707 the output cell-type classifier which was trained randomly initialized. All gene tokens with both  
708 zero and non-zero expression values were used in training. The CLS fine-tuning objective was used  
709 to minimize the classification loss.

710 **Perturbation response prediction** To fine-tune for the perturbation prediction task, we se-  
711 lected highly variable genes and pre-processed the expression values prior to model training. The  
712 parameters of the embedding layers and transformer layers from the pre-trained model were uti-  
713 lized to initialize the fine-tuned model. During fine-tuning, all gene tokens with both zero and  
714 non-zero expression values were included. Two notable changes were adopted for the input in  
715 the perturbation prediction task: First, we used  $\log_{10}$  transformed expression values as input and  
716 target values instead of binned values, to better predict the absolute post-perturbation expression  
717 for this task. Second, we appended a binary condition token at each input gene position to indicate  
718 whether the gene is perturbed. We adopted the perturb-GEP fine-tuning objective with further  
719 modifications to the training setup. Instead of utilizing the masked and unmasked expression val-  
720 ues of the same cell as the input and learning target, we employed a control cell as the input and  
721 the perturbed cell as the target. This was achieved by randomly pairing a non-perturbed control  
722 cell with each perturbed cell to construct the input-target pairs. The input values consisted of all  
723 the non-perturbed gene expression values in the control cells. Consequently, the model learned to  
724 predict the post-perturbation responses based on the control gene expression.

725 **Batch correction on integrating multiple scRNA-seq datasets** Batch effects can be a  
726 major confounder in cell type clustering when the input contains multiple datasets from different  
727 sequencing batches or technologies. Therefore, we aim to correct batch effects while preserving bio-  
728 logical variances when integrating multiple scRNA-seq datasets. For fine-tuning on this integration  
729 task, the common set of gene tokens between the pre-trained foundation model and the current  
730 dataset was retained. We further selected a subset of highly variable genes from the common set  
731 as input. We pre-processed the expression values prior to model training similar to the cell type  
732 annotation task. All pre-trained model weights were used to initialize the fine-tuned model. All  
733 gene tokens with both zero and non-zero expression values were used in training by default. In

734 addition to GEP and GEPC, the ECS, DAR, and DSBN fine-tuning objectives were optimized  
735 simultaneously for enhanced cell contrastive learning and explicit batch correction through reverse  
736 back-propagation and domain-specific normalization.

737 **Integrative representation learning for scMultiomic data** scMultiomic data may contain  
738 different sequencing modalities across experiment batches. We examined two data integration  
739 settings, paired and mosaic, for scMultiomic data. In the paired setting, all samples (cells) share  
740 all the data modalities sequenced. In the mosaic setting, some batches share a few common data  
741 modalities but not all. Due to the presence of additional ATAC and/or protein tokens, we inherited  
742 the trained gene embeddings for RNA data only, and trained the additional token embeddings and  
743 rest of the model from scratch. Only tokens with non-zero expression values were used in training if  
744 the dataset contained additional protein data. Otherwise, both zero and non-zero expression values  
745 were used by default. We used an additional set of modality tokens to indicate the data type of each  
746 token (i.e., gene, region, or protein) and to facilitate the masked gene and value prediction in GEP  
747 and GEPC fine-tuning objectives (Online Methods 4.2.3). The model was optimized with GEP  
748 and GEPC fine-tuning objectives by default. If multiple batches are present, DAR was included  
749 to facilitate multi-modal batch correction.

750 **Gene Regulatory Network Inference** For the gene-embedding-based GRN inference, in the  
751 zero-shot setting, we constructed the gene similarity network from the pretrained scGPT's gene  
752 embeddings based on k-nearest neighbors. In the fine-tuned setting, we constructed the gene  
753 similarity network in a similar manner from the scGPT model fine-tuned on the Immune Human  
754 dataset. Following Ceglia et al. [77]'s pipelines, we further perform Leiden [40] clustering on the  
755 similarity graph and extracted gene programs from gene clusters that consist of five or more genes.

756 For the attention-based target gene selection, we fine-tuned the scGPT blood model on the  
757 Adamson perturbation dataset that consists of 87 CRISPR interference experiments on a leukemia  
758 cell line [36]. We illustrate the target gene selection pipeline in Figure 6A. For each perturbed  
759 gene of interest, we first retrieved two sets of attention maps, perturbed and control, by feeding  
760 the model perturbed versus control cell sets respectively. Note that the raw attention scores  
761 are obtained from all eight attention heads from the last attention layer of the model. The raw  
762 attention scores then go through two rounds of rank normalization, first by row and then by column.  
763 The rank-normalized attention scores are then averaged across eight attention heads to output an  
764 aggregate attention map. This arrives at the final attention map used for the most influenced gene  
765 selection. For each perturbed gene of interest, we select its most influenced genes by ranking the  
766 scores from the final attention map in the column of the perturbed gene. This reflects the intuition  
767 that the columns in the attention map indicate how much the gene of interest affects the other  
768 genes. We offer three most influenced gene selection settings, namely *Control* from the control  
769 attention map, *Perturbed* from the perturbed attention map, and *Difference* from the difference  
770 between the two. The gene targets selected from the control attention map should reflect the basal  
771 pathways that the gene of interest takes part in, whereas the perturbed attention map reflects the  
772 post-perturbation effects. The difference between these two attention maps should highlight the  
773 most changed edges in the gene network from before to after perturbation. See Online Methods  
774 4.7 for more details on gene network analysis and validation.

775        **4.6 Datasets**

776        **CELLxGENE scRNA-seq human PBMC Collection** We collected data for the whole-  
777        human foundation model pre-training from the CELLxGENE portal [28] using the Census API <sup>2</sup>.  
778        We included sequencing protocols of scRNA-seq and snRNA-seq and filtered in samples without  
779        disease conditions. This resulted in sequencing data of 33 million cells. For the pre-training of  
780        the scGPT blood model specifically, we retrieved over 10.3 million human blood and bone marrow  
781        scRNA-seq samples [28]. A total of 65 datasets were collected from CELLxGENE by filtering  
782        on Organism (i.e., Homo sapiens), Tissue (i.e., blood, bone marrow), and Disease (i.e., normal,  
783        COVID-19, influenza). Additionally, we collected 5.7 million cells of various cancer types to train  
784        the pan-cancer model.

785        **Multiple Sclerosis** The multiple sclerosis (M.S.) dataset, originally published by Schirmer et al.  
786        [78], is accessed from EMBL-EBI (<https://www.ebi.ac.uk/gxa/sc/experiments/E-HCAD-35>).  
787        9 healthy control samples and 12 M.S. samples are included in the dataset. We split the control  
788        samples into the reference set for model fine-tuning and held out the M.S. samples as the query  
789        set for evaluation. This setting serves as an example of out-of-distribution data. We excluded  
790        three cell types, B cell, T cell, and oligodendrocyte B, that only existed in the query dataset. The  
791        final cell counts are 7,844 in the training reference set and 13,468 in the query set. The provided  
792        cell-type labels from the original publication were used as ground truth labels for evaluation. The  
793        data processing protocol involved selecting highly variable genes (HVG) to retain 3,000 genes.

794        **Myeloid** The myeloid (Mye.) dataset [33] can be accessed from the Gene Expression Omnibus  
795        (GEO) database using the accession number GSE154763. The dataset consists of nine different  
796        cancer types, but for the purpose of training and evaluating the model, six cancer types were  
797        selected in the reference set for training, while three cancer types were used for the query set. The  
798        reference set contains myeloid cancer types of UCEC, PAAD, THCA, LYM, cDC2, and KIDNEY,  
799        while the query set contains MYE, OV-FTC, and ESCA. The dataset was also randomly subsampled.  
800        The final cell counts are 9,748 in the reference set and 3,430 in the query set. 3,000 highly  
801        variable genes were selected during the data processing.

802        **hPancreas** The hPancreas dataset contains five scRNA-seq datasets of human pancreas cells,  
803        re-processed by Chen et al. [34] for the cell type annotation task. The five datasets were split into  
804        reference and query sets by data sources. The reference set consists of Braon[79] and Muraro[80]  
805        datasets, and the query set consists of Xin[81], Segerstolpe[82], and Lawlor[83] datasets. The  
806        reference and query sets both have 3,000 genes, and ground-truth annotations retained from their  
807        original publications. The reference set contains 10,600 cells of 13 cell groups (alpha, beta, ductal,  
808        acinar, delta, PSC, PP, endothelial, macrophage, mast, epsilon, schwann, and t\_cell). The query  
809        set contains 4,218 cells of 11 cell groups (alpha, beta, ductal, PP, acinar, delta, PSC, endothelial,  
810        epsilon, mast, MHC class II).

811        **PBMC 10K** The PBMC 10K dataset comprises two scRNA-seq batches of human peripheral  
812        blood mononuclear cells (PBMCs) obtained from a healthy donor. The dataset was re-processed  
813        by Gayoso et al. [44], resulting in 3,346 differentially expressed genes. The first batch contains  
814        7,982 cells, while the second batch contains 4,008 cells. The cell groups annotated using Seurat [42]

<sup>2</sup>The Census API is accessible at <https://chanzuckerberg.github.io/cellxgene-census/python-api.html>. It hosts and updates online data releases regularly. We used the release on May 15, 2023

815 consist of 9 categories, namely B cells, CD4 T cells, CD8 T cells, CD14+ Monocytes, Dendritic  
816 Cells, NK cells, FCGR3A+ Monocytes, Megakaryocytes, and Other.

817 **Immune Human** The Immune Human dataset encompasses five scRNA-seq datasets: one de-  
818 rived from human bone marrow and four from human peripheral blood. Various sequencing tech-  
819 nologies were employed, including 10X Genomics, 10X Genomics v2, 10X Genomics v3, and Smart-  
820 seq2. The dataset comprises a total of 33,506 cells and includes 12,303 genes. The ten distinct  
821 batches were defined based on the origin of the donors. The harmonized data contain 16 cell  
822 groups. We used the data re-processed and the annotations provided by Luecken et al. [53].

823 **Perirhinal Cortex** The Perirhinal Cortex dataset includes two distinct samples, drawn from a  
824 larger study by Siletti et al. [45], which originally contained 606 high-quality samples encompassing  
825 ten diverse brain regions. Each of the two selected batches from the Perirhinal Cortex dataset  
826 comprises a substantial number of cells, with the first batch consisting of 8,465 cells and the  
827 second batch containing 9,070 cells. An extensive range of 59,357 genes are incorporated within  
828 these datasets. We have made use of the annotations of ten unique cell types provided in the  
829 original study.

830 **COVID-19** The COVID-19 dataset, derived from work by Lotfollahi et al. [13], is organized into  
831 18 distinct batches and offers a diverse representation of cells from lung tissue, PBMC, and bone  
832 marrow. Initially encompassing 274,346 cells and 18,474 genes, this dataset has been subsampled  
833 to contain a total of 20,000 cells for the purpose of this study. We made use of the annotations  
834 provided by the original study.

835 **Adamson** The Adamson perturbation dataset contains gene expression data from the K562  
836 leukemia cell line perturbed by Pertub-seq [36]. This dataset includes 87 unique one-gene pertur-  
837 bations by CRISPR interference, each replicated in around 100 cells.

838 **Norman** The Norman perturbation dataset contains gene expression data from the K562 leukemia  
839 cell line perturbed by Pertub-seq [37]. This dataset has 131 two-gene perturbations and 105 one-  
840 gene perturbations. Each perturbation is replicated in around 300-700 cells.

841 **10X Multiome PBMC** The 10X Multiome PBMC dataset [47] contains paired single-cell RNA  
842 and ATAC data on human PBMC cells sequenced by the 10X Single Cell Multiome protocol. In this  
843 dataset, all samples came from the same healthy donor. Each cell contains both gene expression and  
844 chromatin accessibility measurements. The processed data by Cao and Gao [14] contains 9,631  
845 cells with read counts from 29,095 genes and 107,194 regions. The annotations include 19 cell  
846 groups (CD14 Mono, CD16 Mono, CD4 Naive, CD4 TCM, CD4 TEM, CD8 Naive, CD8 TEM\_1,  
847 CD8 TEM\_2, HSPC, Intermediate B, MAIT, Memory B, NK, Naive B, Plasma, Treg, cDC, gdT,  
848 and pDC).

849 **BMMC** The BMMC dataset contains paired single-cell RNA and protein abundance measure-  
850 ments on bone marrow mononuclear cells sequenced by the CITE-seq protocol [48]. These cells  
851 came from 12 healthy human donors consisting of 12 batches in this dataset. The processed

852 data contains 90,261 cells with measurements from 14,087 genes and 134 surface proteins. The  
853 annotations consist of 45 detailed immune cell subtypes.

854 **ASAP PBMC** The ASAP PBMC dataset contains four sequencing batches with three data  
855 modalities (gene expression, chromatin accessibility, and protein abundance) [49]. The four batches  
856 each contain 5,023, 3,666, 3,517, and 4,849 cells respectively. In batches 1 and 2, all samples have  
857 4,768 genes and 216 protein measurements from CITE-seq. In batches 3 and 4, all samples have  
858 17,742 regions and the same 216 protein measurements from ASAP-seq. The annotations by  
859 Mimitou et al. [49] contain 4 cell groups (Bcell, Myeloid, NK, and Tcell).

## 860 4.7 Benchmarking Experiment Setup

861 **scRNA-seq cell type annotation** We benchmarked scGPT against two recent transformer-  
862 based cell type annotation methods, scBert [35] and TOSICA [34] on the Mye., M.S., and hPancreas  
863 datasets. For each dataset, as described in the previous section, we used the reference data par-  
864 tition for model training and validation. The predicted cell type labels on the query set were  
865 retrieved for evaluation. We evaluated cell type assignment performance based on four standard  
866 classification metrics, *Accuracy*, *Precision*, *Recall*, and *MacroF1*. *Accuracy*, *Precision*, and  
867 *Recall* are calculated globally for overall performance, whereas *MacroF1* is averaged per class to  
868 increase the weighing of rare cell types. We also reported a normalized confusion matrix with  
869 *Precision* by cell type for additional details. See Supplementary Online Methods S.5 for details  
870 on metric calculations.

871 **scRNA-seq perturbation** We compared scGPT against the recent perturbation prediction  
872 method GEARS [38] and CPA [12]. To ensure consistency, we followed the pre-processing steps  
873 outlined by Roohani, Huang, and Leskovec [38] in their benchmark. It is worth noting that the  
874 steps are different from the settings reported in CPA. To ensure a fair comparison, we trained  
875 all models in the same settings as follows and reported the evaluation results. Initially, gene  
876 expression values were normalized per cell using the total counts across all genes, and a logarithmic  
877 transformation was applied. Subsequently, we selected 5,000 highly variable genes and incorporated  
878 any perturbed genes that were not initially considered into the gene set. In the experiments, for one-  
879 gene perturbations in both datasets Adamson et al. [36] and Norman et al. [37], the perturbations  
880 are split to ensure that test perturbations are not seen in training, i.e., no cells in the training set  
881 has undergone any of the test perturbations. For two-gene perturbations in the Norman et al. [37]  
882 dataset, the train-test split consists of three scenarios with increasing difficulty: (1) 0/2 unseen  
883 genes, (2) 1/2 unseen genes, and (3) 2/2 unseen genes in the training set.

884 To evaluate the accuracy of perturbation prediction, we employed the Pearson correlation  
885 coefficient (*corr*) between the predicted gene expression and the ground-truth expression values.  
886 Additionally, we calculated a variant of the Pearson metric based on the amount of change in  
887 expression post-perturbation compared to the control, denoted as *corr*( $\Delta$ ). We reported these  
888 Pearson metrics on the top 20 genes of most changed expression (*DE* genes). Thus, we presented  
889 two evaluation metrics in total, namely *corr* and *corr*( $\Delta$ ) for the *DE* conditions, respectively.

890 For the cluster-based biological validation, we first retrieved a representative gene expression  
891 profile for each perturbation condition from the scGPT model. scGPT predicted the representative  
892 perturbation response for each perturbation condition from a single vector of sample control gene  
893 expression (i.e., of size  $1 \times M$  genes), obtained by averaging the gene expression of all control cells  
894 in the dataset. The Norman et al. [37] dataset contains 105 unique perturbed genes, which yields

895 a total of 5,565 unique perturbation combinations to predict. We projected the high-dimensional  
896 predicted perturbation responses onto a two-dimensional UMAP. We first compared the UMAP  
897 against the functional groups found in the original publication by Norman et al. [37], where the  
898 236 perturbation experiments were clustered based on ground-truth perturbation responses and  
899 annotated by the marker gene expression for their functional roles. We examined the consistency  
900 between the scGPT-predicted UMAP projections and the functional grouping found in the original  
901 paper. We then analyzed the sub-clusters present in the scGPT-predicted UMAP. With the Leiden  
902 clustering resolution of 0.5, 54 sub-clusters were identified in the UMAP of predicted perturbation  
903 responses. We annotated each cluster with the most occurring perturbed gene as its dominant  
904 gene.

905 For the reverse perturbation prediction task, we selected 20 genes to construct a perturbation  
906 use case from the Norman dataset and to fine-tune and test a new perturbation model. This  
907 subset of 20 genes is selected by maximizing the proportion of ground-truth perturbation data for  
908 both training and test cases based on scGPT's train-test split. This selected subspace contains 39  
909 training cases, 3 validation cases, and 7 test cases out of the 210 unique perturbation combinations.  
910 The rest are unseen cases without experiment results. The reverse perturbation prediction follows  
911 a topK retrieval task setting: we used the predicted responses from all 210 perturbation conditions  
912 as the reference data, and the ground-truth responses from the 7 test cases as the query set. The  
913 goal is to retrieve the top perturbation conditions that generate the most similar responses as to a  
914 query result. For the reference data, instead of having a single representative gene expression profile  
915 for each perturbation condition, we obtained the predicted responses from 40 randomly sampled  
916 control cells for added diversity. This yields a reference database containing 8,400 predicted post-  
917 perturbation gene expression profiles. For each test case of X+Y perturbation, we used the ground-  
918 truth gene expression profiles from all cells that underwent X+Y perturbation as the query set.  
919 For TopK retrieval, we designed an ensemble voting strategy that involves two rounds of selection.  
920 In the first round, each individual query cell selects its top K most similar expression profiles  
921 by Euclidean distance from the reference dataset. In the second round, we rank the candidate  
922 perturbation conditions by the number of votes received from all query cells. We report the top  
923 K most voted perturbation conditions as the predicted source perturbation conditions from the  
924 second round of ranking after ensemble voting. We evaluated the retrieval performance by a  
925 modified topK accuracy metric for correct retrieval (i.e., exact match) and relevant retrieval (i.e.,  
926 matching at least one gene in the actual perturbation combination) as detailed in Supplementary  
927 Online Methods S.5.

928 **scRNA-seq batch integration** In this work, we compared the performance of scGPT with  
929 three other methods, namely Seurat [42], Harmony [43], and scVI [41]. The evaluation covers  
930 batch correction and cell type clustering on four integration datasets: COVID-19 [13], PBMC 10K  
931 [44], and Perirhinal Cortex [45]. Harmony and scVI are highlighted as the top-performing methods  
932 in the recent integration benchmark conducted by Luecken et al. [53]. To ensure a fair comparison,  
933 all methods were provided with the same number of 1,200 highly variable genes as input. Gene  
934 expression values were normalized per cell by considering the total counts across all genes and  
935 subsequently log-transformed. The integrated cell embeddings were obtained after the completion  
936 of training and were used for evaluation.

937 The evaluation of the integrated cell embeddings was performed using biological conservation  
938 metrics proposed by Luecken et al. [53]. These metrics include the normalized mutual information  
939 ( $NMI_{cell}$ ), adjusted Rand index ( $ARI_{cell}$ ), and average silhouette width ( $ASW_{cell}$ ). These  
940 scores measure the consistency between the derived cell type clusters and the ground truth labels.  
941 For easier comparison, we also computed the average of these metrics, referred to as  $AvgBIO$ .  
942 Additionally, we reported the batch correction metrics proposed by Luecken et al. [53] to assess

batch mixing. The batch correction performance was quantified using the inverse of the average silhouette width for batch clustering, denoted as  $ASW_{batch}$ , and the graph connectivity measure, denoted as  $GraphConn$ . We computed  $AvgBATCH$  as the average of  $ASW_{batch}$  and  $GraphConn$  to summarize the batch mixing performance. Furthermore, we introduced an *Overall* score, which is a weighted sum of  $AvgBIO$  and  $AvgBATCH$ , consistent with the approach taken by Luecken et al. [53]. See Supplementary Online Methods S.5 for details of metric calculations.

**scMultiomic integration** We benchmarked scGPT in two integration settings, paired and mosaic, against the recent scMultiomic integration methods Seurat v4 [46], scGLUE [14] and scMoMat [15] respectively. In the paired data integration experiment, we benchmarked scGPT with scGLUE [14] and Seurat v4 [46] on the 10X Multiome PBMC [47] dataset with RNA and ATAC-seq data as the first example. The same 1,200 highly variable genes and 4,000 highly variable peaks were used as input to all methods. We further benchmarked scGPT against Seurat v4 on the BMMC[48] dataset with paired RNA and Protein reads. We did not benchmark scGLUE in this case for fair comparison since the method was not specifically designed to model protein data. Similarly, the same 1,200 highly variable genes and all 134 proteins were used as input. In the mosaic data integration experiment, we benchmarked scGPT with scMoMat [15] on the ASAP PBMC [49] dataset. 1,200 highly variable genes, 4,000 highly variable peaks, and all 216 protein features were used as input to both methods. While keeping the input feature set consistent, we used each method’s custom pre-processing pipeline to normalize the expression values. The integrated cell embeddings were retrieved for evaluation after training.

In all three datasets for both paired and mosaic data integration settings, we evaluated cell embedding quality on the four biological conservation metrics  $NMI_{cell}$ ,  $ARI_{cell}$ ,  $ASW_{cell}$ , and  $AvgBIO$ . Since two of the three datasets, BMMC (paired) and ASAP PBMC (mosaic), contain multiple batches, we further evaluated mixing of different omic batches with the three batch correction metrics  $ASW_{batch}$ ,  $GraphConn$ , and  $AvgBATCH$ . An overall score was also reported on the mosaic integration experiment. See Supplementary Online Methods S.5 for details on metric calculation.

**Gene Regulatory Network Inference** We validated scGPT’s gene embedding similarity network against the known HLA and CD gene networks. For each network, we first defined the related gene set by filtering on gene names with set prefixes (i.e., HLA- and CD-). We then filtered on genes involved in the Immune System R-HSA-168256 pathway from the Reactome 2022 database [54]. For the CD genes, we used the common gene set with the HVGs from the Immune Human dataset for ease of comparison between pre-trained and fine-tuned models. We then extracted gene embeddings of these select genes from the scGPT model and constructed a kNN similarity network. We highlighted sub-networks of strong connections by selecting edges with cosine similarities greater than a certain threshold (i.e., 0.5 for HLA and 0.4 for CD gene network). We then compared the sub-networks against known functional groups from the immune system.

Furthermore, we validated the quality of gene programs extracted by the scGPT model through pathway enrichment analysis. We used each gene program as an input gene list, and selected statistically significant pathways as “pathway hits”. The p-value threshold is adjusted to 0.05 with Bonferroni correction [55] based on the total number of tests performed, i.e., the number of gene programs times the number of pathway tests. We reported the number of pathway hits in the Reactome 2022 database [54]. As a benchmark, we compared the result with the gene programs extracted from the baseline co-expression graph. The co-expression graph was defined by Pearson correlation among genes from their normalized gene expression in the Immune Human dataset. To ensure similar modularity as the scGPT network, we sparsified this graph to a kNN similarity

989 network ( $k=15$ ). Following the same pipeline as scGPT, we identified gene programs from gene  
990 clusters via Leiden clustering. As a sensitivity analysis, we reported the pathway hits for scGPT  
991 and the co-expression method at varying Leiden resolutions of 1, 5, 10, 20, 30, 40, 50, and 60. We  
992 further examined the common and unique pathways identified by each method at Leiden resolution  
993 of 40 to gain more insights into the performance difference.

994 We validated scGPT's attention-based most influenced gene selection method in the ChIP-  
995 Atlas database [56] which contains experiment-validated gene targets for known transcription factors.  
996 We first selected two example transcription factors, *DDIT3* and *BHLHE40*, by cross-checking  
997 the perturbed gene list from the Adamson perturbation dataset [36] with ChIP-Atlas. For each  
998 transcription factor, we validated the top 20 most influenced genes selected by attention in the  
999 *Difference* setting by comparing them against the validated gene targets. Note that in the *Difference*  
1000 setting, the top 20 genes are selected based on post-perturbation changes by examining the  
1001 difference between the perturbed attention map and control attention map. The ground-truth gene  
1002 target list was obtained from ChIP-Atlas by filtering on human genes (hg38) whose transcription  
1003 start sites lie within 10k-bp distance of the peak-call intervals of the transcription factor. We re-  
1004 ported the number of overlaps in the top 20 attention-selected gene targets with the ground-truth  
1005 target genes.

1006 We subsequently compared the three most influenced gene selection methods (i.e., *Control*,  
1007 *Perturbed*, and *Difference*) by examining the overlap between the top 100 genes selected. The  
1008 overlaps and differences of these three top 100 gene sets are visualized in a Venn diagram. We  
1009 further validated the pathways these top genes participate in along with the transcription factor  
1010 in the Reactome database. The pathway hits and the percentage of gene overlap are visualized in  
1011 a heatmap.

## 1012 4.8 Implementation Details

1013 The pre-trained foundation model has an embedding size of 512. It consists of 12 stacked trans-  
1014 former blocks with 8 attention heads each. The fully connected layer has a hidden size of 512. In  
1015 pre-training of the whole-human model using 33M cells, we randomly split the data and used 99.7%  
1016 of the data for training and 0.3% for validation. For the pre-training of other models, including  
1017 the organ-specific models and the pan-cancer model, we randomly split the data and used 97% of  
1018 the data for training and 3% for validation. Note that in pre-training, only genes with non-zero  
1019 expression are input to the model. We set a max input length of 1200. For cells with a number of  
1020 non-zero genes larger than the max input length, 1200 input genes will be randomly sampled at  
1021 each iteration. We set the ratio of genes to generate to be uniformly sampled from three options  
1022 of 0.25, 0.50, and 0.75. The model was optimized by the Adam optimizer, using a mini-batch size  
1023 of 32, at a starting learning rate of 0.0001 and a 0.9 weight decay after each epoch. The model  
1024 was trained for a total of 6 epochs.

1025 For the tasks of scRNA-seq batch integration, cell type annotation, and perturbation prediction,  
1026 we utilized the same model layer configuration inherited from the pre-trained model. During the  
1027 fine-tuning process, we initiated with a learning rate of 0.0001, which decayed to 90% after each  
1028 epoch. For the integration task, the mask ratio for GEP and GEPC was set to 0.4, while the  
1029 parameter  $\beta$  in ECS was set to 0.6. When combined with other losses, ECS was assigned a  
1030 weighting of 10. To divide the datasets into training and validation sets, we employed a ratio of  
1031 9:1. The model was trained for a fixed duration of 15 epochs, and after each epoch, the GEP loss  
1032 value was evaluated on the validation set. The reported results correspond to the model with the  
1033 best validation score.

1034 For the multi-omic integration task, we loaded the gene embeddings from the pre-trained model  
1035 and used the same embedding size of 512 for any new tokens (i.e., gene, ATAC-peak, or protein).  
1036 The main model is set to have 4 stacked transformer blocks with 8 attention heads each, and a  
1037 hidden layer size of 512. All layers are re-initialized except for the pretrained embedding weights.  
1038 Each dataset is split into train and evaluation sets at 9:1 ratio. We used DAR weighing of 1.0 for  
1039 batch integration. We used a starting learning rate of 0.001 and a weight decay of 0.95 after each  
1040 epoch. We trained the model for fixed 25 epochs with batch size 16 and similarly reported the  
1041 best-validated model.

1042 We used the **SCANPY** python library [84] for gene expression pre-processing, including normaliza-  
1043 tion, log-transformation, and highly variable gene selection. We used the EpiScanpy python  
1044 library [85] on chromatin accessibility data for highly variable peak selection. In the scRNA-seq  
1045 batch integration and scMultiomic integration tasks, the evaluation metrics are calculated using  
1046 the implementation in **scib.metrics** by Luecken et al. [53]. In the cell-annotation task, the eval-  
1047 uation metrics are implemented using the **scikit-learn** package. In the GRN inference task, the  
1048 similarity graph construction and Leiden clustering were performed using the **SCANPY** library. The  
1049 pathway enrichment analysis was implemented using the **GSEAp** package [86].

## 1050 Acknowledgement

1051 We would like to express our sincere gratitude to, Dr. Nan Duan, for his invaluable guidance and  
1052 support throughout the project. We appreciate the valuable feedback from Dr. Lin Zhang during  
1053 the writing of the manuscript.

1054 **References**

- 1055 [1] Adam D Silverman, Ashty S Karim, and Michael C Jewett. “Cell-free gene expression: an  
1056 expanded repertoire of applications”. In: *Nature Reviews Genetics* 21.3 (2020), pp. 151–170.
- 1057 [2] Sebastian Preissl, Kyle J Gaulton, and Bing Ren. “Characterizing cis-regulatory elements  
1058 using single-cell epigenomics”. In: *Nature Reviews Genetics* (2022), pp. 1–23.
- 1059 [3] Jun Ding, Nadav Sharon, and Ziv Bar-Joseph. “Temporal modelling using single-cell tran-  
1060 scriptomics”. In: *Nature Reviews Genetics* 23.6 (2022), pp. 355–368.
- 1061 [4] Daniel E Wagner and Allon M Klein. “Lineage tracing meets single-cell omics: opportunities  
1062 and challenges”. In: *Nature Reviews Genetics* 21.7 (2020), pp. 410–427.
- 1063 [5] HCA. *HCA DCP*. <https://data.humancellatlas.org/>. Online; accessed 12 April 2023.  
1064 2023.
- 1065 [6] Aviv Regev et al. “Science forum: the human cell atlas”. In: *elife* 6 (2017), e27041.
- 1066 [7] Xiaoping Han et al. “Mapping the mouse cell atlas by microwell-seq”. In: *Cell* 172.5 (2018),  
1067 pp. 1091–1107.
- 1068 [8] Philipp Angerer et al. “Single cells make big data: New challenges and opportunities in  
1069 transcriptomics”. In: *Current opinion in systems biology* 4 (2017), pp. 85–91.
- 1070 [9] Indhupriya Subramanian et al. “Multi-omics data integration, interpretation, and its appli-  
1071 cation”. In: *Bioinformatics and biology insights* 14 (2020), p. 1177932219899051.
- 1072 [10] Zhen Miao et al. “Multi-omics integration in the age of million single-cell data”. In: *Nature  
1073 Reviews Nephrology* 17.11 (2021), pp. 710–724.
- 1074 [11] Mohammad Lotfollahi, F Alexander Wolf, and Fabian J Theis. “scGen predicts single-cell  
1075 perturbation responses”. In: *Nature methods* 16.8 (2019), pp. 715–721.
- 1076 [12] Mohammad Lotfollahi et al. “Learning interpretable cellular responses to complex pertur-  
1077 bations in high-throughput screens”. In: *BioRxiv* (2021), pp. 2021–04.
- 1078 [13] Mohammad Lotfollahi et al. “Mapping single-cell data to reference atlases by transfer learn-  
1079 ing”. In: *Nature Biotechnology* 40.1 (2022), pp. 121–130.
- 1080 [14] Zhi-Jie Cao and Ge Gao. “Multi-omics single-cell data integration and regulatory inference  
1081 with graph-linked embedding”. In: *Nature Biotechnology* 40.10 (2022), pp. 1458–1466.
- 1082 [15] Ziqi Zhang et al. “scMoMaT jointly performs single cell mosaic integration and multi-modal  
1083 bio-marker detection”. In: *Nature Communications* 14.1 (2023), p. 384.
- 1084 [16] Rishi Bommasani et al. “On the opportunities and risks of foundation models”. In: *arXiv  
1085 preprint arXiv:2108.07258* (2021).
- 1086 [17] Michael Moor et al. “Foundation models for generalist medical artificial intelligence”. In:  
1087 *Nature* 616.7956 (2023), pp. 259–265.
- 1088 [18] OpenAI. *Introducing ChatGPT*. <https://openai.com/blog/chatgpt>. Online; accessed 10  
1089 April 2023. 2023.
- 1090 [19] OpenAI. *GPT-4 Technical Report*. 2023. arXiv: [2303.08774 \[cs.CL\]](https://arxiv.org/abs/2303.08774).
- 1091 [20] OpenAI. *DALL·E 2*. <https://openai.com/product/dall-e-2>. Online; accessed 10 April  
1092 2023. 2023.
- 1093 [21] Suchin Gururangan et al. “Don’t stop pretraining: Adapt language models to domains and  
1094 tasks”. In: *arXiv preprint arXiv:2004.10964* (2020).
- 1095 [22] Chi Sun et al. “How to fine-tune bert for text classification?” In: *Chinese Computational  
1096 Linguistics: 18th China National Conference, CCL 2019, Kunming, China, October 18–20,  
1097 2019, Proceedings 18*. Springer. 2019, pp. 194–206.

- 1098 [23] Xipeng Qiu et al. “Pre-trained models for natural language processing: A survey”. In: *Science China Technological Sciences* 63.10 (2020), pp. 1872–1897.  
1099
- 1100 [24] Jiajia Liu et al. “Machine intelligence in single-cell data analysis: advances and new challenges”. In: *Frontiers in Genetics* 12 (2021), p. 655536.  
1101
- 1102 [25] Sergio Oller-Moreno et al. “Algorithmic advances in machine learning for single-cell expres-  
1103 sion analysis”. In: *Current Opinion in Systems Biology* 25 (2021), pp. 27–33.  
1104
- 1105 [26] Yuge Ji et al. “Machine learning for perturbational single-cell omics”. In: *Cell Systems* 12.6  
(2021), pp. 522–537.  
1106
- 1107 [27] Ashish Vaswani et al. “Attention is all you need”. In: *Advances in neural information  
processing systems* 30 (2017).  
1108
- 1109 [28] Chanzuckerberg Initiative. *CZ CELLxGENE Discover*. <https://cellxgene.cziscience.com/>. Online; accessed 26 December 2022. 2022.  
1110
- 1111 [29] Leland McInnes, John Healy, and James Melville. “Umap: Uniform manifold approxima-  
1112 tion and projection for dimension reduction”. In: *arXiv preprint arXiv:1802.03426* (2018).  
1113
- 1114 [30] Allen W Zhang et al. “Probabilistic cell-type assignment of single-cell RNA-seq for tumor  
1115 microenvironment profiling”. In: *Nature methods* 16.10 (2019), pp. 1007–1015.  
1116
- 1117 [31] Dvir Aran et al. “Reference-based analysis of lung single-cell sequencing reveals a transi-  
1118 tional profibrotic macrophage”. In: *Nature immunology* 20.2 (2019), pp. 163–172.  
1119
- 1120 [32] Jurrian K De Kanter et al. “CHETAH: a selective, hierarchical cell type identification  
1121 method for single-cell RNA sequencing”. In: *Nucleic acids research* 47.16 (2019), e95–e95.  
1122
- 1123 [33] Sijin Cheng et al. “A pan-cancer single-cell transcriptional atlas of tumor infiltrating myeloid  
1124 cells”. In: *Cell* 184.3 (2021), pp. 792–809.  
1125
- 1126 [34] Jiawei Chen et al. “Transformer for one stop interpretable cell type annotation”. In: *Nature  
1127 Communications* 14.1 (2023), p. 223.  
1128
- 1129 [35] Wenchuan Wang et al. “scBERT: a Large-scale Pretrained Deep Langurage Model for Cell  
1130 Type Annotation of Single-cell RNA-seq Data”. In: *bioRxiv* (2021).  
1131
- 1132 [36] Britt Adamson et al. “A multiplexed single-cell CRISPR screening platform enables sys-  
1133 tematic dissection of the unfolded protein response”. In: *Cell* 167.7 (2016), pp. 1867–1882.  
1134
- 1135 [37] Thomas M Norman et al. “Exploring genetic interaction manifolds constructed from rich  
1136 single-cell phenotypes”. In: *Science* 365.6455 (2019), pp. 786–793.  
1137
- 1138 [38] Yusuf Roohani, Kexin Huang, and Jure Leskovec. “GEARS: Predicting transcriptional out-  
1139 comes of novel multi-gene perturbations”. In: *bioRxiv* (2022).  
1140
- 1141 [39] Mohammad Lotfollahi et al. “Predicting cellular responses to complex perturbations in  
high-throughput screens”. In: *Molecular Systems Biology* (2023), e11517.  
1142
- 1143 [40] Vincent A Traag, Ludo Waltman, and Nees Jan Van Eck. “From Louvain to Leiden: guar-  
1144 anteeing well-connected communities”. In: *Scientific reports* 9.1 (2019), p. 5233.  
1145
- 1146 [41] Romain Lopez et al. “Deep generative modeling for single-cell transcriptomics”. In: *Nature  
1147 methods* 15.12 (2018), pp. 1053–1058.  
1148
- 1149 [42] Rahul Satija et al. “Spatial reconstruction of single-cell gene expression data”. In: *Nature  
1150 biotechnology* 33.5 (2015), pp. 495–502.  
1151
- 1152 [43] Ilya Korsunsky et al. “Fast, sensitive and accurate integration of single-cell data with Har-  
1153 mony”. In: *Nature methods* 16.12 (2019), pp. 1289–1296.  
1154
- 1155 [44] Adam Gayoso et al. “A Python library for probabilistic analysis of single-cell omics data”.  
In: *Nature Biotechnology* 40.2 (2022), pp. 163–166.  
1156

- 1142 [45] Kimberly Siletti et al. “Transcriptomic diversity of cell types across the adult human brain”.  
1143 In: *bioRxiv* (2022), pp. 2022–10.
- 1144 [46] Yuhan Hao et al. “Integrated analysis of multimodal single-cell data”. In: *Cell* 184.13 (2021),  
1145 pp. 3573–3587.
- 1146 [47] Darren A Cusanovich et al. “Multiplex single-cell profiling of chromatin accessibility by  
1147 combinatorial cellular indexing”. In: *Science* 348.6237 (2015), pp. 910–914.
- 1148 [48] Malte D Luecken et al. “A sandbox for prediction and integration of dna, rna, and proteins  
1149 in single cells”. In: *35th Conference on Neural Information Processing Systems (NeurIPS  
1150 2021) Track on Datasets and Benchmarks*. 2021.
- 1151 [49] Eleni P Mimitou et al. “Scalable, multimodal profiling of chromatin accessibility, gene ex-  
1152 pression and protein levels in single cells”. In: *Nature biotechnology* 39.10 (2021), pp. 1246–  
1153 1258.
- 1154 [50] Aditya Pratapa et al. “Benchmarking algorithms for gene regulatory network inference from  
1155 single-cell transcriptomic data”. In: *Nature methods* 17.2 (2020), pp. 147–154.
- 1156 [51] Paola Cruz-Tapias, John Castiblanco, and Juan-Manuel Anaya. “Major histocompatibility  
1157 complex: antigen processing and presentation”. In: *Autoimmunity: From Bench to Bedside  
1158 [Internet]*. El Rosario University Press, 2013.
- 1159 [52] Philip S Norman. “Immunobiology: The immune system in health and disease”. In: *Journal  
1160 of Allergy and Clinical Immunology* 96.2 (1995), p. 274.
- 1161 [53] Malte D Luecken et al. “Benchmarking atlas-level data integration in single-cell genomics”.  
1162 In: *Nature methods* 19.1 (2022), pp. 41–50.
- 1163 [54] Reactome. *Reactome Pathway Database: Home*. <https://reactome.org/>. 2022.
- 1164 [55] Eric W Weisstein. “Bonferroni correction”. In: <https://mathworld.wolfram.com/> (2004).
- 1165 [56] Zhaonan Zou et al. “ChIP-Atlas 2021 update: a data-mining suite for exploring epigenomic  
1166 landscapes by fully integrating chip-seq, ATAC-seq and Bisulfite-seq data”. In: *Nucleic acids  
1167 research* 50.W1 (2022), W175–W182.
- 1168 [57] Huan Yang et al. “ATF6 is a critical determinant of CHOP dynamics during the unfolded  
1169 protein response”. In: *Iscience* 23.2 (2020), p. 100860.
- 1170 [58] Hiderou Yoshida et al. “ATF6 activated by proteolysis binds in the presence of NF-Y (CBF)  
1171 directly to the cis-acting element responsible for the mammalian unfolded protein response”.  
1172 In: *Molecular and cellular biology* 20.18 (2000), pp. 6755–6767.
- 1173 [59] National Library of Medicine. *Bhlhe40 basic helix-loop-helix family, member e40 [Mus mus-  
1174 culus (house mouse)]*. <https://www.ncbi.nlm.nih.gov/gene/20893>. Online; accessed 29  
1175 May 2023. 2023.
- 1176 [60] Jared Kaplan et al. “Scaling laws for neural language models”. In: *arXiv preprint arXiv:2001.08361*  
1177 (2020).
- 1178 [61] Abhishek Sarkar and Matthew Stephens. “Separating measurement and expression models  
1179 clarifies confusion in single-cell RNA sequencing analysis”. In: *Nature genetics* 53.6 (2021),  
1180 pp. 770–777.
- 1181 [62] Ashraful Haque et al. “A practical guide to single-cell RNA-sequencing for biomedical re-  
1182 search and clinical applications”. In: *Genome medicine* 9.1 (2017), pp. 1–12.
- 1183 [63] Malte D Luecken and Fabian J Theis. “Current best practices in single-cell RNA-seq anal-  
1184 ysis: a tutorial”. In: *Molecular systems biology* 15.6 (2019), e8746.
- 1185 [64] Jacob Devlin et al. “Bert: Pre-training of deep bidirectional transformers for language un-  
1186 derstanding”. In: *arXiv preprint arXiv:1810.04805* (2018).

- 1187 [65] Tri Dao et al. “FlashAttention: Fast and Memory-Efficient Exact Attention with IO-Awareness”.  
1188 In: *arXiv preprint arXiv:2205.14135* (2022).
- 1189 [66] Sinong Wang et al. “Linformer: Self-attention with linear complexity”. In: *arXiv preprint*  
1190 *arXiv:2006.04768* (2020).
- 1191 [67] Angelos Katharopoulos et al. “Transformers are rnns: Fast autoregressive transformers  
1192 with linear attention”. In: *International Conference on Machine Learning*. PMLR. 2020,  
1193 pp. 5156–5165.
- 1194 [68] Yinhan Liu et al. “Roberta: A robustly optimized bert pretraining approach”. In: *arXiv*  
1195 *preprint arXiv:1907.11692* (2019).
- 1196 [69] Alec Radford et al. “Improving language understanding by generative pre-training”. In:  
1197 (2018).
- 1198 [70] Alec Radford et al. “Language models are unsupervised multitask learners”. In: *OpenAI*  
1199 *blog* 1.8 (2019), p. 9.
- 1200 [71] Tom Brown et al. “Language models are few-shot learners”. In: *Advances in neural infor-*  
1201 *mation processing systems* 33 (2020), pp. 1877–1901.
- 1202 [72] Sébastien Bubeck et al. *Sparks of Artificial General Intelligence: Early experiments with*  
1203 *GPT-4*. 2023. arXiv: [2303.12712 \[cs.CL\]](https://arxiv.org/abs/2303.12712).
- 1204 [73] Chundi Liu et al. “Guided similarity separation for image retrieval”. In: *Advances in Neural*  
1205 *Information Processing Systems* 32 (2019).
- 1206 [74] Michael Eisenstein. “Single-cell RNA-seq analysis software providers scramble to offer solu-  
1207 tions.” In: *Nature Biotechnology* 38.3 (2020), pp. 254–257.
- 1208 [75] Hoa Thi Nhu Tran et al. “A benchmark of batch-effect correction methods for single-cell  
1209 RNA sequencing data”. In: *Genome biology* 21.1 (2020), pp. 1–32.
- 1210 [76] Yaroslav Ganin and Victor Lempitsky. “Unsupervised domain adaptation by backpropaga-  
1211 tion”. In: *International conference on machine learning*. PMLR. 2015, pp. 1180–1189.
- 1212 [77] Nicholas Ceglia et al. “GeneVector: Identification of transcriptional programs using dense  
1213 vector representations defined by mutual information”. In: *bioRxiv* (2022), pp. 2022–04.
- 1214 [78] Lucas Schirmer et al. “Neuronal vulnerability and multilineage diversity in multiple sclero-  
1215 sis”. In: *Nature* 573.7772 (2019), pp. 75–82.
- 1216 [79] Maayan Baron et al. “A single-cell transcriptomic map of the human and mouse pancreas  
1217 reveals inter-and intra-cell population structure”. In: *Cell systems* 3.4 (2016), pp. 346–360.
- 1218 [80] Mauro J Muraro et al. “A single-cell transcriptome atlas of the human pancreas”. In: *Cell*  
1219 *systems* 3.4 (2016), pp. 385–394.
- 1220 [81] Yurong Xin et al. “RNA sequencing of single human islet cells reveals type 2 diabetes genes”.  
1221 In: *Cell metabolism* 24.4 (2016), pp. 608–615.
- 1222 [82] Åsa Segerstolpe et al. “Single-cell transcriptome profiling of human pancreatic islets in  
1223 health and type 2 diabetes”. In: *Cell metabolism* 24.4 (2016), pp. 593–607.
- 1224 [83] Nathan Lawlor et al. “Single-cell transcriptomes identify human islet cell signatures and  
1225 reveal cell-type-specific expression changes in type 2 diabetes”. In: *Genome research* 27.2  
1226 (2017), pp. 208–222.
- 1227 [84] F Alexander Wolf, Philipp Angerer, and Fabian J Theis. “SCANPY: large-scale single-cell  
1228 gene expression data analysis”. In: *Genome biology* 19.1 (2018), pp. 1–5.
- 1229 [85] Anna Danese et al. “EpiScanpy: integrated single-cell epigenomic analysis”. In: *Nature Com-*  
1230 *munications* 12.1 (2021), p. 5228.
- 1231 [86] Zhuoqing Fang, Xinyuan Liu, and Gary Peltz. “GSEAPy: a comprehensive package for per-  
1232 forming gene set enrichment analysis in Python”. In: *Bioinformatics* 39.1 (2023), btac757.

- 1233 [87] Alexey Dosovitskiy et al. “An image is worth 16x16 words: Transformers for image recog-  
1234 nition at scale”. In: *arXiv preprint arXiv:2010.11929* (2020).
- 1235 [88] John Jumper et al. “Highly accurate protein structure prediction with AlphaFold”. In:  
1236 *Nature* 596.7873 (2021), pp. 583–589.
- 1237 [89] Hongru Shen et al. “Generative pretraining from large-scale transcriptomes: Implications  
1238 for single-cell deciphering and clinical translation”. In: *bioRxiv* (2022).
- 1239 [90] William Connell, Umair Khan, and Michael J Keiser. “A single-cell gene expression language  
1240 model”. In: *arXiv preprint arXiv:2210.14330* (2022).
- 1241 [91] Christina V Theodoris et al. “Transfer learning enables predictions in network biology”. In:  
1242 *Nature* (2023), pp. 1–9.
- 1243 [92] Tim Stuart et al. “Comprehensive integration of single-cell data”. In: *Cell* 177.7 (2019),  
1244 pp. 1888–1902.
- 1245 [93] Jialin Liu et al. “Jointly defining cell types from multiple single-cell datasets using LIGER”.  
1246 In: *Nature protocols* 15.11 (2020), pp. 3632–3662.
- 1247 [94] Chloe X Wang, Lin Zhang, and Bo Wang. “One Cell At a Time (OCAT): a unified framework  
1248 to integrate and analyze single-cell RNA-seq data”. In: *Genome biology* 23.1 (2022), pp. 1–  
1249 25.
- 1250 [95] Diederik P Kingma and Max Welling. “Auto-encoding variational bayes”. In: *arXiv preprint*  
1251 *arXiv:1312.6114* (2013).
- 1252 [96] Adam Gayoso et al. “Joint probabilistic modeling of single-cell multi-omic data with to-  
1253 talVI”. In: *Nature methods* 18.3 (2021), pp. 272–282.
- 1254 [97] Kemal Inecik et al. “MultiCPA: Multimodal Compositional Perturbation Autoencoder”. In:  
1255 *bioRxiv* (2022), pp. 2022–07.
- 1256 [98] Lucas Seninge et al. “VEGA is an interpretable generative model for inferring biological  
1257 network activity in single-cell transcriptomics”. In: *Nature communications* 12.1 (2021),  
1258 pp. 1–9.
- 1259 [99] Anjun Ma et al. “Deepmaps: Single-cell biological network inference using heterogeneous  
1260 graph transformer”. In: *bioRxiv* (2021).
- 1261 [100] Lars Buitinck et al. “API design for machine learning software: experiences from the scikit-  
1262 learn project”. In: *ECML PKDD Workshop: Languages for Data Mining and Machine*  
1263 *Learning*. 2013, pp. 108–122.

1264

## Supplementary Notes

1265

### S.1 Context-Specific Pre-training and Its Influence on Integration Performance

1267

We pre-trained scGPT on cell atlases including all human cell types, envisioning that it contributes to specific downstream applications primarily via fine-tuning. Since downstream applications usually focus on a small subset of tissues or cell types, a natural question for us is whether it would better contribute to a specific fine-tuning task via the pretraining on all cells or a context-specific pretraining. To be specific, for the downstream fine-tuning on specific *contexts* of certain cell types, we are interested in comparing the contributions of three different pretrained models: (1) scGPT (whole-human), which is the model pretrained generally on all human cell types; (2) in-context models, which during pretraining have seen similar cell types as in the downstream applications; (3) out-of-context models, which are pretrained largely on different tissues or cell types from the downstream applications. To conduct this comparison, we tested a range of pre-trained models on the scRNA-seq data integration task. These pre-trained models were originally trained using distinct tissue-specific datasets, including lung, blood, heart, kidney, brain, pancreas, intestine, and an all-inclusive, whole-human cells dataset. In particular, we subsampled from the original whole-human dataset to generate a dataset of 13.2 million cells, aligning it in size with the blood (10.3 million cells) and brain (13.2 million cells) datasets for a more direct comparison of context impact. We employed each of the eight pre-trained models to perform data integration on the COVID-19 dataset [13], followed by a comparative performance analysis. Given its diverse cellular composition, including Lung, PBMC, and Bone Marrow cells, this dataset provides an ideal platform for investigating the effects of employing pre-trained models from different cellular contexts.

1268

1269

1270

1271

1272

1273

1274

1275

1276

1277

1278

1279

1280

1281

1282

1283

1284

1285

1286

1287

Our process yielded notable results, revealing a clear correlation between the relevance of the model context used in the pre-training initiatives and their subsequent performance on the COVID-19 dataset. Supplementary Figure S8 graphically illustrates these findings, showcasing the average *AvgBIO* score along with the standard error derived from five integration experiments for each pre-trained model (Panel A). Moreover, the UMAP visualization (Panel B) presents an in-depth view of the cell embeddings colored by cell types, substantiating the quality of the learned representations and visually validating the models' integration performance. Notably, the top performers in this analysis were models pre-trained on whole-human, blood, and lung datasets, which correspond closely to the cell types present in the COVID-19 dataset.

1288

1289

1290

1291

1292

1293

1294

1295

1296

1297

1298

1299

1300

1301

1302

1303

1304

1305

In particular, even though the brain pre-trained model was trained on a substantial dataset of 13 million cells, it trailed in performance by 8% compared to the blood pre-trained model with a similar dataset size. This gap in performance sheds light on the importance of cellular context relevance. Specifically, the cellular context of the blood model aligns more closely with the COVID-19 dataset, which includes immune cells, bone marrow cells, lung cells, and PBMCs. Thus, it becomes evident that the alignment of the cellular context in the pre-training phase plays a critical role in achieving superior results for downstream data integration tasks, even when datasets of similar sizes are compared. In light of our findings, the whole-human pre-trained model, embodying a vast spectrum of cell types, consistently demonstrates robust performance across diverse analyses.

1306

1307

1308

1309

Our investigation underlined the significance of cellular context in single-cell RNA-seq data integration tasks. In certain circumstances, when the cellular context of the target dataset aligns with the tissue-specific pre-trained models, these models can excel. Overall, while it is essential to consider the cellular context, the whole-human pre-trained model emerges as a versatile and

1310 reliable option for a wide range of applications.

1311

## S.2 Benchmarking results on downstream tasks

Dataset	Model	Classification Metrics			
		<i>Accuracy</i>	<i>Precision</i>	<i>Recall</i>	<i>MacroF1</i>
Myeloid	scGPT (fine-tuned)	<b>0.642</b>	<b>0.366</b>	<b>0.347</b>	<b>0.346</b>
	scGPT (from-scratch)	0.606	0.304	0.339	0.309
	TOSICA	0.488	0.316	0.276	0.275
	scBert	0.525	0.331	0.323	0.298
Multiple Sclerosis	scGPT (fine-tuned)	<b>0.856</b>	<b>0.729</b>	<b>0.720</b>	<b>0.703</b>
	scGPT (from-scratch)	0.798	0.660	0.623	0.600
	scBert	0.785	0.604	0.624	0.599
	TOSICA	0.758	0.664	0.585	0.578
hPancreas	scGPT (fine-tuned)	<b>0.968</b>	<b>0.735</b>	<b>0.725</b>	<b>0.718</b>
	scGPT (from-scratch)	0.936	0.665	0.668	0.622
	TOSICA	0.960	0.661	0.681	0.656
	scBert	0.964	0.699	0.689	0.685

Table S1: Cell Type Annotation Benchmark Results. scGPT was benchmarked with TOSICA [34] and scBert [35] on the Myeloid (Mye.), Multiple Sclerosis (M.S.), and hPancreas [34] datasets for cell type annotation performance. We present four classification evaluation metrics *Accuracy*, *Precision*, *Recall*, and *MacroF1*. See metric details in Supplementary Online Methods S.5.

Dataset	Model	Biological Conservation				Batch Correction			<b>Overall</b>
		<b>AvgBIO</b>	<i>NMI<sub>cell</sub></i>	<i>ARI<sub>cell</sub></i>	<i>ASW<sub>cell</sub></i>	<b>AvgBATCH</b>	<i>ASW<sub>batch</sub></i>	<i>GraphConn</i>	
COVID-19 [13]	scGPT (fine-tuned)	<b>0.504</b>	0.659	0.400	0.452	<b>0.850</b>	0.826	0.874	<b>0.642</b>
	scGPT (from-scratch)	0.450	0.602	0.318	0.429	0.744	0.712	0.776	0.567
	scVI [41]	0.502	0.638	0.408	0.461	0.838	0.833	0.844	0.637
	Seurat [42]	0.413	0.513	0.289	0.437	0.790	0.799	0.781	0.564
	Harmony [43]	0.327	0.482	0.185	0.313	0.680	0.642	0.720	0.468
PBMC 10K [44]	scGPT (fine-tuned)	<b>0.821</b>	0.850	0.873	0.740	0.923	0.950	0.895	<b>0.862</b>
	scGPT (from-scratch)	0.723	0.738	0.793	0.639	0.893	0.919	0.867	0.791
	scVI	0.753	0.819	0.847	0.592	<b>0.947</b>	0.967	0.928	0.831
	Seurat	0.724	0.808	0.722	0.641	0.940	0.960	0.920	0.810
	Harmony	0.784	0.860	0.902	0.591	0.940	0.975	0.906	0.846
Perirhinal Cortex [45]	scGPT (fine-tuned)	<b>0.899</b>	0.930	0.919	0.848	0.930	0.898	0.964	0.911
	scGPT (from-scratch)	0.889	0.886	0.895	0.886	0.884	0.892	0.875	0.887
	scVI	0.869	0.980	0.990	0.637	0.966	0.939	0.992	0.908
	Seurat	0.878	0.914	0.897	0.822	0.965	0.938	0.992	0.913
	Harmony	0.890	0.960	0.960	0.749	<b>0.975</b>	0.957	0.992	<b>0.924</b>

Table S2: scRNA-seq Integration Benchmark Results. scGPT was benchmarked with scVI [41], Seurat [42], and Harmony [43] on the COVID-19 (18 batches) [13], PBMC 10K (2 batches) [44] and Perirhinal Cortex (2 batches) [45] datasets for cell type clustering and batch correction performance. We present three aggregate scores *AvgBIO*, *AvgBATCH*, and *Overall*. These aggregate scores were calculated from three detailed biological conservation metrics ( $NMI_{cell}$ ,  $ARI_{cell}$ ,  $ASW_{cell}$ ) and two batch correction metrics ( $ASW_{batch}$ ,  $GraphConn$ ). See metric details in Supplementary Online Methods [S.5](#)

Dataset	Model	Biological Conservation				Batch Correction			<b>Overall</b>
		<b>AvgBIO</b>	<i>NMI</i> <sub>cell</sub>	<i>ARI</i> <sub>cell</sub>	<i>ASW</i> <sub>cell</sub>	<b>AvgBATCH</b>	<i>ASW</i> <sub>batch</sub>	<i>GraphConn</i>	
10X Multiome PBMC [47] (Paired RNA+ATAC)	scGPT (fine-tuned)	<b>0.758</b>	0.807	0.822	0.645	-	-	-	-
	scGPT (from-scratch)	0.728	0.775	0.759	0.651	-	-	-	-
	scGLUE [14]	0.747	0.815	0.806	0.619	-	-	-	-
	Seurat v4 [46]	0.722	0.784	0.691	0.691	-	-	-	-
BMMC [48] (Paired RNA+Protein)	scGPT (fine-tuned)	<b>0.697</b>	0.783	0.725	0.582	<b>0.871</b>	0.834	0.908	<b>0.766</b>
	scGPT (from-scratch)	0.696	0.777	0.718	0.593	0.822	0.789	0.854	0.746
	Seurat v4 [46]	0.600	0.737	0.470	0.594	0.678	0.685	0.671	0.631
ASAP PBMC [49] (Mosaic RNA+ATAC+Protein)	scGPT (fine-tuned)	<b>0.587</b>	0.645	0.469	0.648	<b>0.951</b>	0.909	0.992	<b>0.732</b>
	scGPT (from-scratch)	0.508	0.549	0.286	0.689	0.941	0.891	0.991	0.681
	scMoMat [15]	0.546	0.448	0.557	0.633	0.916	0.849	0.983	0.667

Table S3: scMultiomic Integration Benchmark Results. For the paired 10X Multiome PBMC[47] dataset, scGPT was benchmarked with scGLUE[14] and Seurat v4[46] for cell type clustering performance evaluated on four biological conservation metrics. The data has only one technical batch. Batch correction metrics are not applicable to this setting. For the paired BMMC[48] and mosaic ASAP PBMC[49] datasets, scGPT was benchmarked with Seurat v4 and scMoMat [15] respectively on cell type clustering and multi-omic integration performance, evaluated on eight biological conservation and batch correction metrics.

Common Pathways (N = 15)	Unique Pathways from Co-expression (N = 6)	Unique Pathways from scGPT (N = 22)
APC/C-mediated Degradation Of Cell Cycle Proteins R-HSA-174142	APC/C/Cdc20 Mediated Degradation Of Cyclin B R-HSA-174048	Adaptive Immune System R-HSA-1280218
APC/C/Cdc20 Mediated Degradation Of Mitotic Proteins R-HSA-176409	Cell Cycle Checkpoints R-HSA-69620	Antiviral Mechanism By IFN-stimulated Genes R-HSA-1169410
Activation Of APC/C And APC/C/Cdc20 Mediated Degradation Of Mitotic Proteins R-HSA-176814	ESR-mediated Signaling R-HSA-8939211	Classical Antibody-Mediated Complement Activation R-HSA-173623
Cell Cycle R-HSA-1640170	Estrogen-dependent Gene Expression R-HSA-9018519	Costimulation By CD28 Family R-HSA-388841
Cell Cycle, Mitotic R-HSA-69278	Resolution Of Sister Chromatid Cohesion R-HSA-2500257	Creation Of C4 And C2 Activators R-HSA-166786
Cytokine Signaling In Immune System R-HSA-1280215	Separation Of Sister Chromatids R-HSA-2467813	Downstream TCR Signaling R-HSA-202424
Immune System R-HSA-168256		G1/S Transition R-HSA-69206
Interferon Signaling R-HSA-909733		G2/S-specific Transition R-HSA-69205
Interferon Signaling R-HSA-913531		Generation Of Second Messenger Molecules R-HSA-202433
M Phase R-HSA-48886		ISG15 Antiviral Mechanism R-HSA-1169408
Mitotic Anaphase R-HSA-68882		Initial Triggering Of Complement R-HSA-166663
Mitotic Metaphase And Anaphase R-HSA-2555396		Interferon Gamma Signaling R-HSA-877300
NGF-stimulated Transcription R-HSA-9031628		MHC Class II Antigen Presentation R-HSA-2132295
Neutrophil Degranulation R-HSA-6798695		Mitotic G1 Phase And G1/S Transition R-HSA-453279
Phosphorylation Of APC/C R-HSA-176412		Nuclear Events (Kinase- And Transcription Factor Activation) R-HSA-198725
		PD-1 Signaling R-HSA-389948
		Phosphorylation Of CD3 And TCR Zeta Chains R-HSA-202427
		RHO GTPases Activate PAKs R-HSA-5627123
		Smooth Muscle Contraction R-HSA-445355
		TCR Signaling R-HSA-202403
		Translocation Of ZAP-70 To Immunological Synapse R-HSA-202430

Table S4: Comparison of Common and Unique Pathways Identified by scGPT and the Co-expression Network From the Reactome Database. The enriched pathways from gene programs extracted by both methods at Leiden resolution 40 are listed here for comparison, corresponding to the Venn diagram in Figure 5 E. The 14 immune-related pathways uniquely identified by scGPT are highlighted in bold.

1312        **S.3 Enhancing Speed and Decreasing Memory Usage in Fine-tunings**

1313        In an attempt to hasten the fine-tuning phase and render scGPT more accessible for users, we  
1314        explored a variety of fine-tuning methods in the context of the scRNA-seq integration task. The  
1315        pre-trained weights from the whole-human dataset were employed to initialize our entire model.  
1316        As the standard practice, the baseline Full fine-tune procedure involves gradient updates for all  
1317        model parameters and includes all zero-expressed genes. We undertook experiments that involved  
1318        freezing the embedding layers and omitting zero-expressed genes during fine-tuning. From data  
1319        presented in table S5, we noticed a significant drop in the training time per epoch as well as in GPU  
1320        Memory usage throughout the fine-tuning process. Specifically, the removal of zero-expressed genes  
1321        resulted in a substantial reduction in our model’s maximum sequence length to approximately 40  
1322         $\sim 60\%$  of its initial length, effectively halving both the time spent on training epochs and peak  
1323        GPU Memory utilization. Furthermore, by freezing the embedding layer, we achieved an additional  
1324        reduction in Peak GPU Memory usage by 1GB, a slight increase in training speed, while preserving  
1325        a comparable AvgBio score.

Dataset	Fine-tuning Option	Fine-tuning Metrics		<b>AvgBio</b>
		Avg Epoch Time(s)	Peak GPU Mem(G)	
COVID-19 [13]	Default	93.89	18.784	<b>0.504</b>
	Accelerated	<b>28.84</b>	<b>7.848</b>	0.473
PBMC 10K [44]	Default	56.91	18.248	0.821
	Accelerated	<b>26.40</b>	<b>8.088</b>	<b>0.828</b>
Perirhinal Cortex [45]	Default	81.00	18.248	<b>0.899</b>
	Accelerated	<b>37.22</b>	<b>7.816</b>	<b>0.899</b>

Table S5: Benchmarking Results for scRNA-seq Integration Speed Enhancement Techniques. scGPT was evaluated based on different fine-tuning strategies on four datasets: COVID-19 (18 batches) [13], PBMC 10K (2 batches) [44], and Perirhinal Cortex (2 batches) [45]. These evaluations were performed to assess cell type clustering and batch correction performance. This table encapsulates two system metrics: the average duration of training per epoch and the maximum GPU memory usage on an A100 GPU. The resulting *AvgBio* score is also presented for performance comparisons.

1326

## S.4 Comparison to existing approaches

1327

**Transformers for modelling single-cell sequencing data.** Transformer models employing self-attention mechanisms [27] have demonstrated remarkable success in the field of natural language processing (NLP) [64], computer vision [87], and protein folding prediction [88]. However, there have been few efforts to incorporate the transformer architecture into single-cell biology and its related applications. Shen et al. [89] utilize a transformer decoder setup to learn the sequence of the names of highly expressed genes, but they do not take into account the actual sequenced expression abundance, resulting in the loss of crucial biological information. scBERT [35] and TOSICA [34] used BERT-like architectures [64] to train cell embeddings but only applied the model on the supervised task of cell annotation. Similarly, Connell, Khan, and Keiser [90] utilized transformer encoders mainly to predict genetic perturbation responses. To our best knowledge, scGPT is one of the first methods to provide a generative pre-trained transformer foundation model for multiple single-cell analysis tasks.

1328

1329

1330

1331

1332

1333

1334

1335

1336

1337

1338

1339

**Pre-training on large cell atlases** Although the idea of employing pre-training and fine-tuning on a wide range of downstream tasks as a unified framework remains largely unexplored, several works have attempted to use transfer learning on specific tasks. scArches [13] devised a transfer-learning-based approach for reference mapping by pre-training a conditional variational autoencoder (VAE) on the reference datasets. However, the scale of the reference datasets remains limited, and the VAE-based architecture does not incorporate attention computation. On the other hand, scBERT [35] is pre-trained on 1 million cells with a BERT architecture. However, the downstream application focuses on cell type annotation only, thus restricting the generalizability of the pre-training and fine-tuning strategy. A recent work, Geneformer [91], has extended pretrained transformers beyond cell type annotation to gene network analysis, but the work didn't demonstrate abilities for perturbation response prediction or multi-omic integration. scGPT has compiled an unprecedented scale of pre-training data and evaluated on a diverse range of downstream tasks, which presents the pre-training and fine-tuning strategy as a unified framework for versatile single-cell analysis.

1340

1341

1342

1343

1344

1345

1346

1347

1348

1349

1350

1351

1352

1353

**Learning cell and gene representation for scRNA-seq on downstream tasks.** Cell representation learning facilitates a variety of downstream tasks such as cell type annotation, multi-omic integration, and perturbation prediction. A popular framework Seurat [42, 92] employs nearest-neighbor-based alignment to remove batch effect via linear transformation in the embedding space. LIGER [93] and OCAT [94] use matrix factorization to extract latent cell embeddings. Recently, Deep Learning methods and especially VAE-based generative models have gained increasing popularity, as they generate deep embeddings via non-linear transformations through neural networks [95]. scVI [41] learns latent cell representations by reconstructing original gene expression via variational inference. TotalVI [96], scGen [11], CPA [12] and MultiCPA [97] utilized similar models and extended the application to multi-omics and perturbation prediction. On the other hand, gene representation learning also supports many downstream tasks including gene regulatory network and functional pathway analysis. As an example, GeneVector [77] detects gene-gene functional relations by factorizing the co-expression and mutual information matrix of the sequencing readout. VEGA [98] utilizes a sparse VAE architecture to encode gene network activities for added interpretability. DeepMAPS [99] utilizes graph neural networks to encode cell and gene nodes for related tasks. Despite the importance of the two branches of research in cell and gene embedding learning, few approaches have worked on jointly learning both. scGPT stands out as an approach to effectively learn both embeddings of cells and genes jointly in a shared architecture.

1371            **S.5 Evaluation Metric Calculations**

1372            **S.5.1 Cell Type Assignment**

1373            We used the standard classification metrics *Accuracy*, *Precision*, *Recall*, and *MacroF1* to evaluate  
1374            cell type assignment performance. The *Accuracy*, *Precision*, *Recall*, and *MacroF1* scores are  
1375            calculated from true positives (*tp*), false positives (*fp*), true negatives (*tn*), and false negatives  
1376            (*fn*) globally or averaged per class.

1377            The *Accuracy*, *Precision* and *Recall* scores are calculated globally:

$$\text{Accuracy} = \frac{tp}{tp + fp + tn + fn}, \quad \text{Precision} = \frac{tp}{tp + fp}, \quad \text{Recall} = \frac{tp}{tp + fn} .$$

1378            The *MacroF1* score is calculated per cell type *c* first and averaged across cell types:

$$\text{MacroF1} = \sum_{c \in C} \frac{F1_c}{N_c}, \quad \text{where } F1_c = \frac{2 \times \text{Precision}_c \times \text{Recall}_c}{\text{Precision}_c + \text{Recall}_c} .$$

1379            The above metrics are calculated using `scikit-learn`'s implementations [100].

1380            **S.5.2 Reverse Perturbation - Predicting driving gene perturbations with TopK Re-**  
1381            **trieval**

1382            We employed two modified topK retrieval accuracy metrics to assess the reverse perturbation  
1383            prediction performance. The hit rate of correct predictions calculates the proportion of test cases  
1384            where the topK retrieved experiments contain the target (i.e., query) condition. For example, for  
1385            each test case of target condition X+Y, if the topK retrieved experiments contain X+Y, we count  
1386            this test case as a hit. We also reported a relaxed topK accuracy metric for relevant retrievals with  
1387            one-gene overlap. The percentage of test cases with relevant predictions calculates the proportion  
1388            of test cases where the topK retrieved experiments contain any cases with a one-gene overlap with  
1389            the target condition. For example, for the same test case X+Y, if the topK retrieved experiments  
1390            contain X, Y, X+A, A+X, Y+A, or A+Y, we count this test case as a hit. This relaxed metric  
1391            aims to provide added interpretability for scGPT's choices of retrieval.

1392            **S.5.3 Single-cell integration**

1393            We adopted the evaluation metric calculations outlined by Luecken et al. [53] in their benchmark  
1394            study. Each metric is described below.

1395            **Normalized Mutual Information**

1396            To quantify the concurrence between the cell type labels based on ground truth and the Lou-  
1397            vain cluster labels obtained from integrated cell embeddings, we computed the normalized mutual  
1398            information (NMI) score. The Louvain clustering was conducted across resolutions ranging from  
1399            0.1 to 2, with increments of 0.1. The best score will be selected. The NMI score for cell types,

1400 referred to as  $NMI_{cell}$ , ranges between 0 and 1, where a higher score indicates a better match of  
1401 cell types.

1402 **Adjusted Rand Index**

1403 The adjusted rand index (ARI) was employed to assess both the agreement between the anno-  
1404 tated labels and the MNI-optimized Louvain clusters. Furthermore, the rand index was adjusted  
1405 to account for randomly correct labels. The ARI score for cell types, denoted as  $ARI_{cell}$ , ranges  
1406 from 0 to 1, where 0 corresponds to random labeling and 1 represents a perfect match.

1407 **Average Silhouette Width**

1408 The silhouette width assesses the relationship between a cell's within-cluster distances and its  
1409 distances to the closest cluster boundaries. By averaging the silhouette widths of all cells, we  
1410 calculate the average silhouette width (ASW) score. This score ranges from -1 to 1, where a score  
1411 of 1 indicates well-separated clusters, while scores from -1 to 0 suggest overlapping clusters and  
1412 misclassification.

1413 For evaluating cell type clustering, we compute the ASW score based on cell type labels,  
1414 represented as  $ASW_{cell}$ . To obtain this score, we utilize the following formula:

$$ASW_{cell} = (ASW_C + 1)/2$$

1415 Here,  $C$  represents the cell types.

1416 Regarding batch mixing evaluation, we calculate the ASW score considering batch labels and  
1417 adjust it by subtracting 1. This score is denoted as  $ASW_{batch}$ . The calculation is as follows:

$$ASW_{batch} = 1 - |ASW_B|$$

1418 Both  $ASW_{cell}$  and  $ASW_{batch}$  have values between 0 and 1. Higher scores indicate better  
1419 cell-type clustering or batch-mixing performance.

1420 **Graph Connectivity**

1421 The graph connectivity metric quantifies the average proportion of cells within each cell type  
1422 that are connected through a kNN (k-nearest neighbors) graph. For every cell identity  $c$  in the  
1423 set  $C$ , we compute the size of the largest connected component using kNN among cells exclusively  
1424 belonging to identity  $c$ . This value is divided by the total number of cells with identity  $c$  to obtain  
1425 a normalized measure. The  $GraphConn$  score is then reported as the average across all cell  
1426 types:

$$GraphConn = \frac{1}{|C|} \sum_{c \in C} \frac{|LCC(G_c^{kNN})|}{N_c}$$

1427 Here,  $LCC$  represents the largest connected component, and  $N$  denotes the number of cells of  
1428 each celltype.

1429 **Aggregated Metrics**

1430 The aggregated metric ***AvgBIO*** calculates the average of biological conservation metrics:

$$\text{AvgBIO} = (\text{ARI}_{cell} + \text{NMI}_{cell} + \text{ASW}_{cell})/3$$

1431 Similarly, the aggregated metric ***AvgBATCH*** computes the average of batch mixing metrics:

$$\text{AvgBATCH} = (\text{ASW}_{batch} + \text{GraphConn})/2$$

1432 In accordance with the convention established in [53], an ***Overall*** metric is derived as the  
1433 weighted average of ***AvgBIO*** and ***AvgBATCH***:

$$\text{AvgBATCH} = 0.6 * \text{AvgBIO} + 0.4 * \text{AvgBATCH}$$

1434

## Supplementary Figures

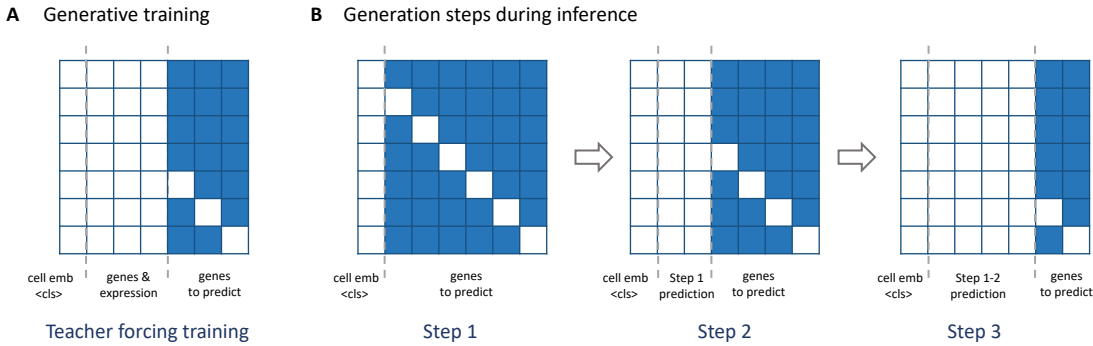


Figure S1: The scGPT Attention Mask. The masked positions are colored in blue, and the unmasked positions in white. These masked and unmasked positions correspond to the  $M \times M$  attention map for  $M$  input tokens. The row indices correspond to queries and columns correspond to keys. In the self-attention computation of transformers, the attention scores on the masked positions will be removed. The token identity associated with each column is annotated below, namely “cell emb  $<\text{cls}>$ ” for cell embedding, “genes & expression” for known genes, and “genes to predict” for unknown genes. (A) scGPT attention mask in training where only query gene and the known genes participate in attention computation. (B) After training, the attention mask at each step during the iterative process of scGPT cell-prompt generation.

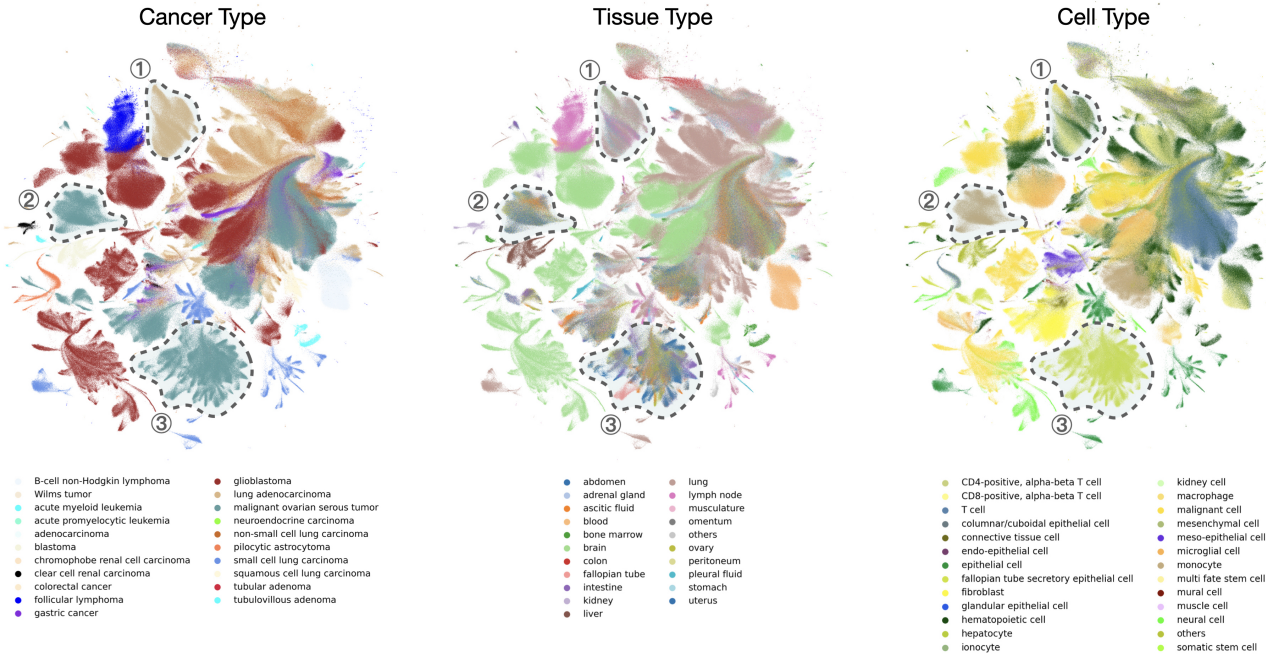


Figure S2: UMAP of 3 million cancer cells using the cell embeddings from the pre-trained pan-cancer model. From left to right, the colors indicate the cancer types, tissue types, and cell types. We observed that the model is able to generate cell embeddings revealing the difference in cancer and cell types primarily, exemplified by the outlined three regions.

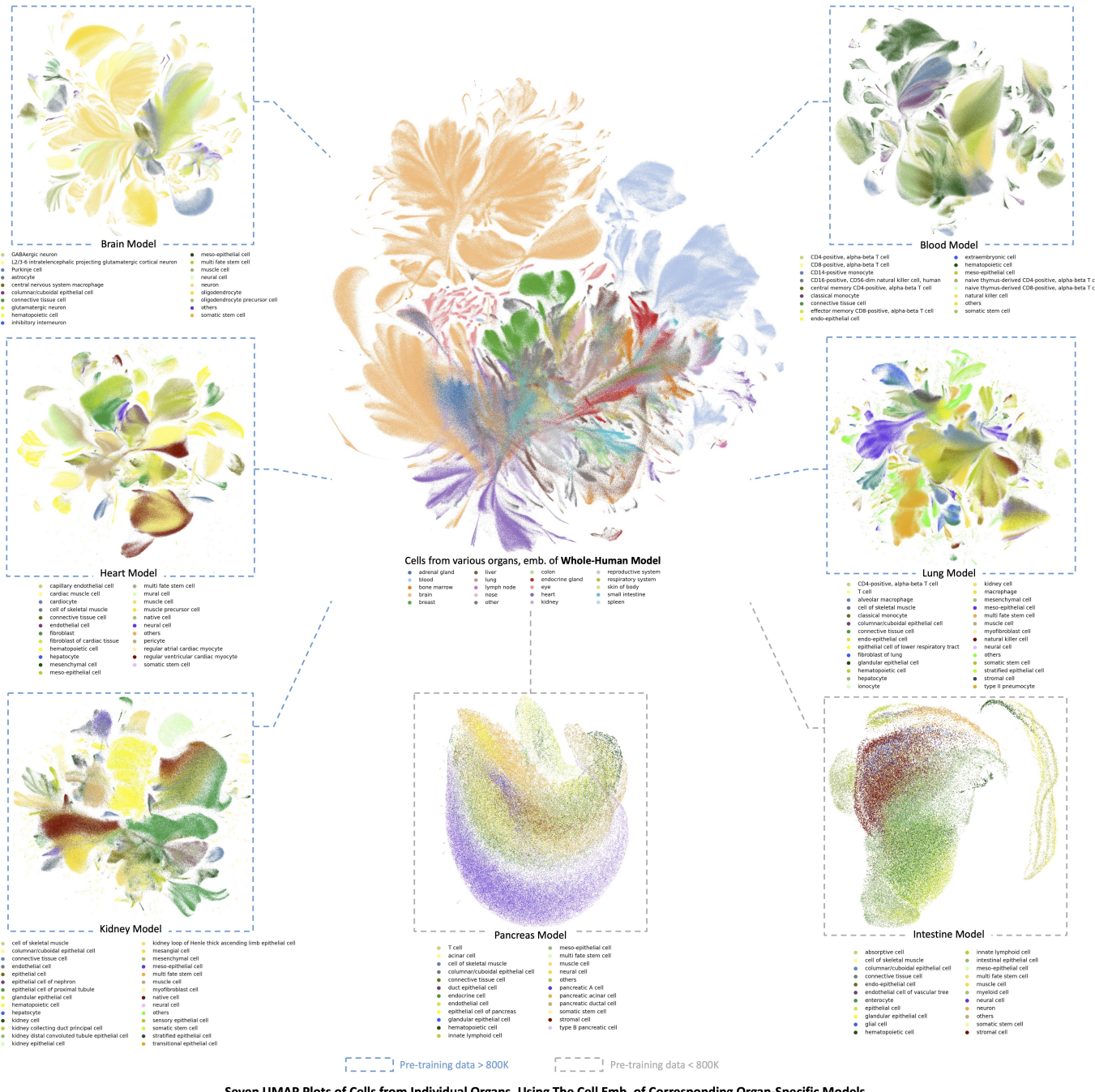


Figure S3: Organ-specific models. (*Center*) The UMAP visualization of selected 3 million collected normal human cells using the cell embeddings from the pre-trained scGPT whole-human model. Cells are colored by the organs of origin. (*Around*) The UMAP visualization of cells from each organ using the cell embeddings from the corresponding organ-specific models. The colors in each image indicate major cell types. For example, the top left UMAP visualizes brain cell embeddings from the scGPT model that was specifically pre-trained on brain cells. The outline color of each UMAP plot indicates whether the size of the organ-specific training data is larger than 800,000 cells (blue) or not (grey). We observed that models trained on sufficient data (i.e.,  $> 800,000$  cells) could generate decent cell embeddings that can separate major cell types.

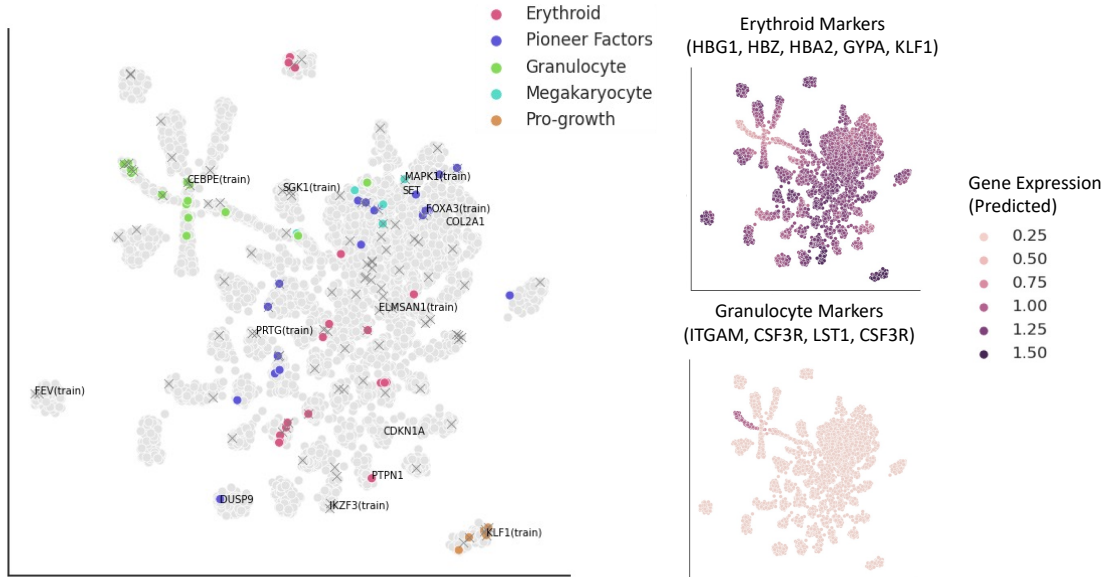


Figure S4: Visualization of Annotated Functional Groups by Norman et al. [37]. (*Left*) UMAP visualization of perturbation condition embeddings colored by *functional groups* on the left. Crosses indicate perturbations that have been tested experimentally in the original study. Colored dots indicate perturbation conditions with annotations. (*Right*) UMAP visualization of perturbation condition embeddings colored by average predicted marker gene expression on the right for the Erythroid and Granulocyte cell groups.

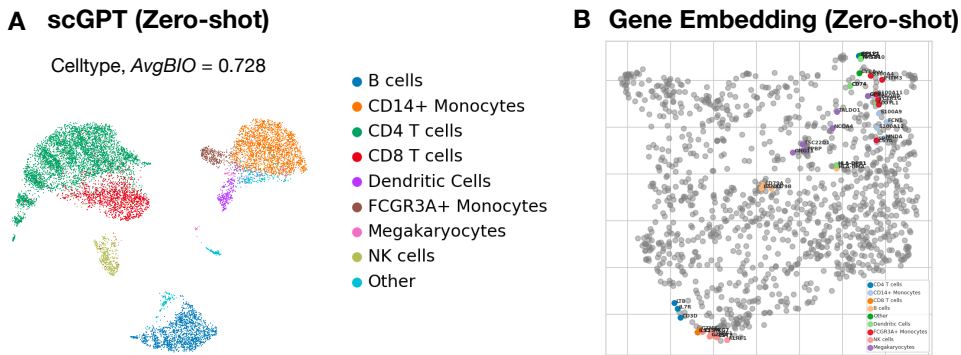


Figure S5: Visualization of the scGPT cell and gene embeddings on the PBMC 10K dataset, using the pre-trained model without fine-tuning (i.e., zero-shot). (A) UMAP visualization of cell embeddings colored by *cell types*. (B) UMAP visualization of gene embeddings. The highly variable genes corresponding to major *celltype* were colored accordingly.

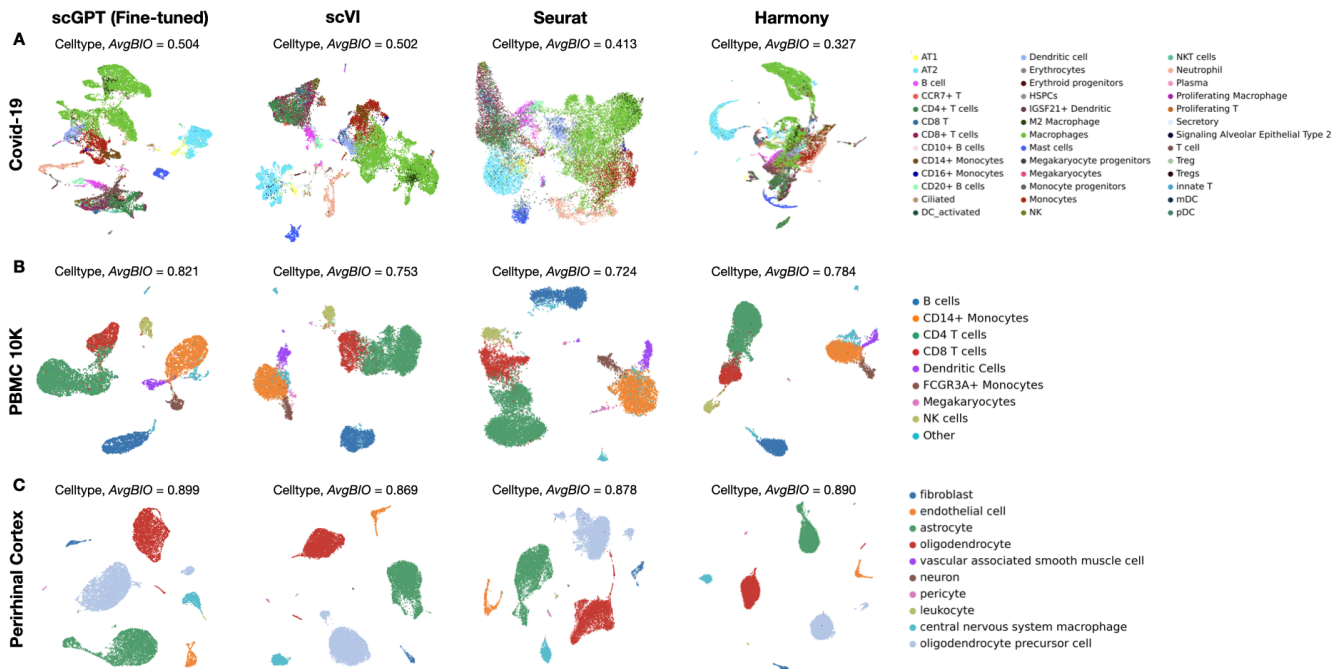


Figure S6: (A,B,C) Benchmark of the fine-tuned scGPT model with scVI [41], Seurat [42], and Harmony [43] on the COVID-19 (18 batches) [13], PBMC 10K (2 batches) [44], and Perirhinal Cortex (2 batches) [45] datasets for cell type clustering performance upon batch integration. The UMAP plot of learned cell embeddings was colored by *cell types*.

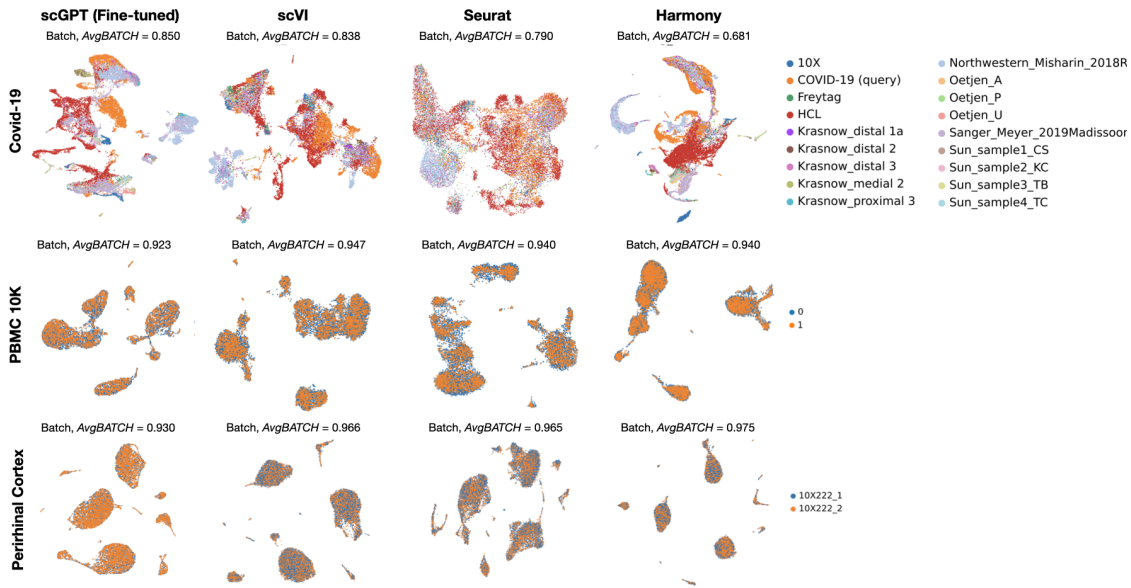


Figure S7: Benchmark of scGPT with scVI [41], Seurat [42], and Harmony [43] on the COVID-19 (18 batches) [13], PBMC 10K (2 batches) [44], and Perirhinal Cortex (2 batches) [45] Datasets for Batch Correction. UMAP visualization of cell embeddings colored by *sequencing batches*.

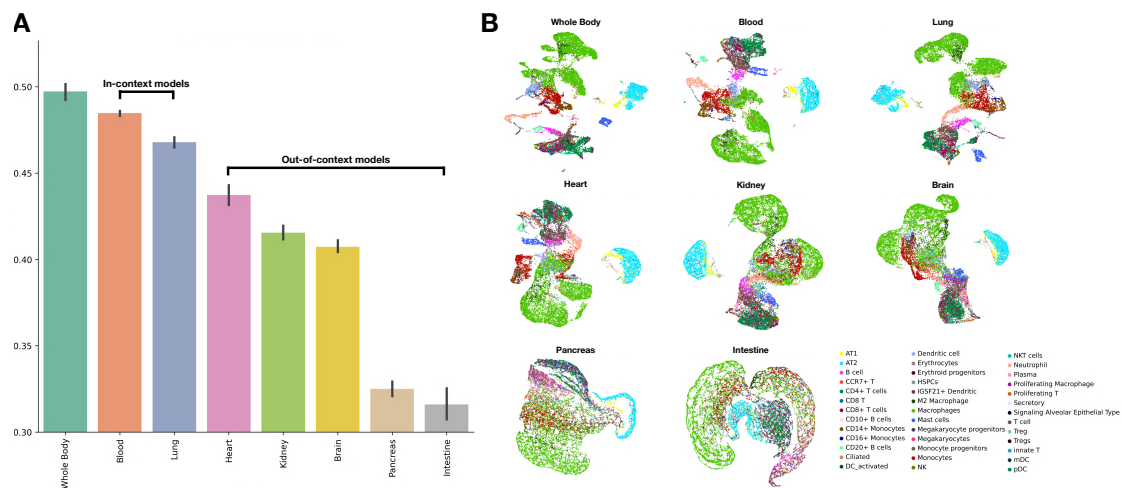


Figure S8: scRNA-seq batch integration results on the COVID-19 dataset (comprising 18 batches) [13], with fine-tuning applied on each of our tissue-specific pre-training models. The COVID-19 dataset comprises a range of samples, including those derived from COVID-19, lung, bone marrow, and PBMC data, reflecting its cellular context. (A) Illustration of the average *AvgBIO* score along with the standard error derived from five scRNA-seq integration experiments for each pre-training model. The *AvgBIO* score provides a quantitative measure of the efficacy of each pre-trained model in integrating batches. The models are ordered by their average score, highlighting the potential of tissue-specific pre-training in improving the performance of integration. In-context models (Blood and Lung), which align with the cell types in the target dataset, are separated from out-of-context models (Heart, Brain, Kidney, Pancreas, Intestine) by annotation brackets, highlighting the influence of cellular context on the integration performance. (B) UMAP visualization of the cell embeddings, colored by *cell types*, achieved by fine-tuning each of the tissue-specific pre-training models. The plots depict the quality of learned representations in the context of cell type diversity, offering visual confirmation of the models' integration capabilities.